Central Lancashire Online Knowledge (CLoK)

Title	Herschel Gould Belt Survey Observations of Dense Cores in the Cepheus Flare Clouds
Type	Article
URL	https://clok.uclan.ac.uk/35855/
DOI	https://doi.org/10.3847/1538-4357/abc016
Date	2020
Citation	Di Francesco, James, Keown, Jared, Fallscheer, Cassandra, André, Philippe, Ladjelate, Bilal, Konyves, Vera, Men'shchikov, Alexander, Stephens-Whale, Shaun, Nguyen-Luong, Quang et al (2020) Herschel Gould Belt Survey Observations of Dense Cores in the Cepheus Flare Clouds. The Astrophysical Journal, 904 (2). p. 172. ISSN 0004-637X
Creators	Di Francesco, James, Keown, Jared, Fallscheer, Cassandra, André, Philippe, Ladjelate, Bilal, Konyves, Vera, Men'shchikov, Alexander, Stephens-Whale, Shaun, Nguyen-Luong, Quang, Martin, Peter, Sadavoy, Sarah, Pezzuto, Stefano, Fiorellino, Eleonora, Benedettini, Milena, Schneider, Nicola, Bontemps, Sylvain, Arzoumanian, Doris, Palmeirim, Pedro, Kirk, Jason and Ward-Thompson, Derek

It is advisable to refer to the publisher's version if you intend to cite from the work.
https://doi.org/10.3847/1538-4357/abc016

For information about Research at UCLan please go to http://www.uclan.ac.uk/research/

CrossMark

Herschel Gould Belt Survey Observations of Dense Cores in the Cepheus Flare Clouds

James Di Francesco[1] , Jared Keown[2] , Cassandra Fallscheer[3], Philippe André[4] , Bilal Ladjelate[5], Vera Könyves[6] ,
Alexander Men'shchikov[4], Shaun Stephens-Whale[2], Quang Nguyen-Luong[7], Peter Martin[8] , Sarah Sadavoy[9],
Stefano Pezzuto[10] , Eleonora Fiorellino[10] , Milena Benedettini[10] , Nicola Schneider[11,12] , Sylvain Bontemps[12],
Doris Arzoumanian[13], Pedro Palmeirim[13] , Jason M. Kirk[6] , and Derek Ward-Thompson[6]

[1] National Research Council of Canada, Herzberg Astronomy & Astrophysics Research Centre, 5071 West Saanich Road, Victoria, BC V9E 2E7, Canada
james.difrancesco@nrc-cnrc.gc.ca
[2] University of Victoria, Department of Physics & Astronomy, PO Box 1700 STN CSC, Victoria, BC V8W 2Y2, Canada
[3] Central Washington University, Department of Physics, 400 E. University Way, Ellensburg, WA 98926-7422, USA
[4] Laboratoire AIM Paris-Saclay, CEA/IRFU CNRS/INSU Université Paris Diderot, F-91191 Gif-sur-Yvette, France
[5] Instituto de Radioastronomía Milimétrica, Avenida Divina Pastora, 7, Núcleo Central, E-18012 Granada, Spain
[6] Jeremiah Horrocks Institute, University of Central Lancashire, Preston, PR1 2HE, UK
[7] Graduate School of Science, Nagoya City University, Mizuho-ku, Nagoya, 467-8501, Japan
[8] University of Toronto, Department of Astronomy & Astrophysics, 50 St. George Street, Toronto, ON M5S 3H4, Canada
[9] Queen's University, Department of Physics, Engineering and Astronomy, 64 Bader Lane, Kingston, ON K7L 3N6, Canada
[10] Istituto di Astrofisica e Planetologia Spaziali, via del Fosso del Cavaliere 100, I-00133 Roma, Italy
[11] I. Physikalisches Institut, Universität zu Köln, Zülpicher Str. 77, D-50937, Köln, Germany
[12] OASU/LAB, Université de Bordeaux, F-33615, Pessac, France
[13] Instituto de Astrofisica e Ciencias do Espaco, Universidade do Porto, CAUP, Rua das Estrelas, PT4150-762, Porto, Portugal

Abstract

We present Herschel SPIRE and PACS maps of the Cepheus Flare clouds L1157, L1172, L1228, L1241, and L1251, observed by the Herschel Gould Belt Survey of nearby star-forming molecular clouds. Through modified blackbody fits to the SPIRE and PACS data, we determine typical cloud column densities of $(0.5–1.0) \times 10^{21}\,\mathrm{cm}^{-2}$ and typical cloud temperatures of 14–15 K. Using the *getsources* identification algorithm, we extract 832 dense cores from the SPIRE and PACS data at 160–500 μm. From placement in a mass versus size diagram, we consider 303 to be candidate prestellar cores, and 178 of these to be "robust" prestellar cores. From an independent extraction of sources at 70 μm, we consider 25 of the 832 dense cores to be protostellar. The distribution of background column densities coincident with candidate prestellar cores peaks at $(2–4) \times 10^{21}\,\mathrm{cm}^{-2}$. About half of the candidate prestellar cores in Cepheus may have formed as a result of the widespread fragmentation expected to occur within filaments of "transcritical" line mass. The lognormal robust prestellar core mass function (CMF) drawn from all five Cepheus clouds peaks at 0.56 $M_\odot$ and has a width of ~0.5 dex, similar to that of Aquila's CMF. Indeed, the width of Cepheus's aggregate CMF is similar to the stellar system initial mass function (IMF). The similarity of CMF widths in different clouds and the system IMF suggests a common, possibly turbulent origin for seeding the fluctuations that evolve into prestellar cores and stars.

Unified Astronomy Thesaurus concepts: Interstellar medium (847); Young stellar objects (1834); Star formation (1569); Protostars (1302); Initial mass function (796); Dense interstellar clouds (371); Molecular clouds (1072); Interstellar filaments (842)

Supporting material: figure set, machine-readable tables

1. Introduction

Understanding the process of star formation is a major cornerstone of modern astrophysics. Stars form primarily in giant molecular clouds, when gas overdensities called "dense cores" become unstable to gravitational collapse. Indeed, the process of star formation is likely inextricably linked to the process of dense core formation in molecular clouds. Dense cores are generally 0.1 pc in size or less, 10 K in temperature, and $10^4–10^5\,\mathrm{cm}^{-3}$ in density. Dense cores that have not formed a young stellar object (YSO) and are arguably not bound by their own gravity are called "starless cores." Those dense cores that are arguably bound and hence more likely to collapse are called "prestellar cores" (see Di Francesco et al. 2007;

Ward-Thompson et al. 2007). By examining the populations of starless and prestellar cores in molecular clouds, we can gain insight into how star formation is proceeding in those clouds, i.e., the potential yield of new stars into the Galaxy.

The Herschel Gould Belt Survey (HGBS; André et al. 2010) is a key program to use the PACS and SPIRE continuum instruments of the ESA Herschel Space Observatory to map nearby molecular clouds within 500 pc distance and identify their populations of cores via emission from dust mixed with the dense gas. Given the low temperatures of cores, they emit most brightly at the far-infrared and submillimeter wavelengths Herschel was designed to observe. Indeed, the location of Herschel at the Sun−Earth L2 point allowed it to map the emission from such wavelengths without a bright and highly opaque atmosphere being simultaneously observed. The resulting Herschel maps have been unprecedented in their sensitivity to faint, diffuse emission from cold dust in molecular clouds.

Table 1
Details of Herschel Observations

Field	Reference Coordinates (J2000)	Observation Date	ObsID
L1157	310.260070672, +67.7461347933	2010 Jan 28	1342189843, 1342189844
L1172	315.713555697. +67.9081656174	2009 Dec 28	1342188652, 1342188653
L1228	314.040903913, +77.4053720025	2010 Jun 21	1342198861, 1342198862
L1241	330.152030576, +76.8345462465	2009 Dec 28	1342188679, 1342186680
L1251	338.041909837, +75.2584297386	2009 Dec 28	1342188654, 1342186655
L1251	338.041909837, +75.2584297386	2010 Jan 25	1342189663, 1342189664

Key results from the HGBS so far include the identification of the ubiquity of filamentary substructure in molecular clouds, the close association of prestellar cores in some clouds with filaments of average column density greater than a fiducial threshold or transition of $\sim 7 \times 10^{21}$ cm^{-2}, and the universality of the lognormal morphology of the prestellar core mass function (André et al. 2014). Much of these results have come from observation of the relatively active Aquila Rift star-forming cloud (André et al. 2010; Könyves et al. 2015). The Gould Belt consists of a variety of star-forming clouds, however, and it is important to explore star formation in different environments to gauge how universal the early findings of the HGBS are.

In this paper, we present the HGBS observations of the Cepheus Flare clouds, L1157, L1172/74, L1228, L1241, and L1251. These clouds are located in a loose association of compact dark clouds scattered across $\sim 10°$ of sky at high decl. ($\sim 68°$–$78°$). These Cepheus clouds were selected to be part of the HGBS given their known star formation activity (see Kun et al. 2008, for a review) and relatively close distances to the Sun. L1172/74 (hereafter L1172) in particular is home to the bright NGC 7023 nebula (aka the Iris Nebula) that is illuminated by the Herbig Ae star HD 200775. L1241 and L1251 lie within the Cepheus Flare Shell, an expanding supernova bubble about 10° in radius that may have enhanced star formation in those clouds. Indeed, L1228 may be coincident with the edge of the Cepheus Flare Shell itself. L1157 and L1172, however, appear to be exterior to the Shell. At the time of their selection, the Cepheus clouds were estimated to be 200–300 pc distant. Dzib et al. (2018), however, recently used GAIA DR2 data to determine a new distance of 358 ± 32 pc to the Cepheus Flare, which we adopt for all five clouds examined in this paper.

Kirk et al. (2009) presented the results of the Spitzer Gould Belt Survey observations of several clouds in the Cepheus Flare, including L1172, L1228, L1241, and L1251 but not L1157. The Spitzer data from the near- to mid-infrared IRAC and mid-infrared MIPS instruments largely sampled the more evolved YSO population of the Cepheus clouds, i.e., Class I, flat, Class II (T Tauri), and Class III objects. Notably, 93 YSOs were found in the L1172, L1228, and L1251 clouds in total. Beyond a single Class III object, L1241 was found to be without YSOs down to a limit of 0.06 $L_\odot$. More recently, Pattle et al. (2017) presented the results of the JCMT Gould Belt Survey of the Cepheus clouds, including L1172, L1228, and L1251 but not L1157 or L1241. This survey included SCUBA-2 observations of high column density regions at 850 μm and largely sampled the most compact, cold structures in these clouds, such as prestellar cores and Class 0 objects. From ratios of numbers of starless cores to Class II objects, Pattle et al. (2017) suggested that low-ratio L1228 was a less active

star-forming cloud while high-ratio L1172 and L1251 were more active.

With Herschel data, we have access to far-infrared/submillimeter emission from the Cepheus clouds of high sensitivity and resolution over a wide range of spatial scales, sampling both faint and diffuse and bright and compact emission sources. With such capability, we can examine filamentary structure in these clouds previously undetected from ground-based emission or extinction map studies. Moreover, we can provide a census of the starless cores, prestellar cores, and protostellar cores in these five clouds and corresponding catalogs of their observed and physical properties. Moreover, given the lower column densities previously estimated for these clouds, these observations provide a counterpoint to observations of more active star-forming clouds in the Gould Belt. A recent analysis of other lower column density star-forming clouds in Lupus was recently presented by Benedettini et al. (2018).

This paper is organized as follows: In Section 2, we describe the observations and data reduction performed on the Herschel data. In Section 3, we present the results of the data, including column density and temperature maps, and source extractions. In Section 4, we discuss core formation in the low column density regime of the Cepheus clouds and discuss the core mass functions of the Cepheus clouds as a whole and separately. In Section 5, we provide a summary and conclusions. The paper also contains three appendices: in Appendix A, we provide the images of all five clouds at 70, 160, 250, 350, and 500 μm; in Appendix B, we provide the criteria applied to sources detected by the *getsources* algorithm for reliability; and in Appendix C, we list the information provided in online material, including catalogs of the observed and derived physical properties of all dense cores identified in the Cepheus clouds studied and thumbnail images of each core at 70–500 μm and in H$_2$ column density.

2. Observations and Data Reduction

Each Cepheus field was observed simultaneously with the Herschel Space Observatory's Spectral and Photometric Imaging Receiver (SPIRE) and Photodetector Array Camera and Spectrometer (PACS) instruments in parallel mode, as part of the HGBS Key Program (André et al. 2010).[14] Further information on Herschel, SPIRE, and PACS can be found in Pilbratt et al. (2010), Griffin et al. (2010), and Poglitsch et al. (2010), respectively. Table 1 summarizes the Herschel observations of the five Cepheus fields, giving the name of each field, the J2000 coordinates of the reference position of each map, the observational date (in UT), and the Observation

---

[14] For information on the HGBS, see http://gouldbelt-herschel.cea.fr.

IDs (ObsIDs), respectively. Each field was observed twice, with scans made in roughly perpendicular position angles, at a scanning speed of $60''\,\mathrm{s}^{-1}$. Fortuitously, L1251 was actually observed four times, i.e., two pairs of orthogonal scans.

The Herschel data were reduced using HIPE (Ott 2011), following the standard HGBS "first generation catalog" prescriptions. We refer readers to the first HGBS data catalog paper (Könyves et al. 2015) for details on the data reduction steps. (See also other recent HGBS data catalog papers by Marsh et al. 2016; Bresnahan et al. 2018; Benedettini et al. 2018; Könyves et al. 2020; Ladjelate et al. 2020). We provide a brief sketch of the steps below.

For the PACS data at 70 and 160 μm, HIPE version 9.0.3063 was used. After standard steps of masking bad pixels, applying flat-field corrections and nonlinear responsivity corrections to the data, deglitching cosmic-ray hits, and applying a high-pass filter of scan-leg length, the PACS images were produced with the IDL-based mapmaker, Scanamorphos version 20 (Roussel 2013). As in Könyves et al. (2015), the absolute point-source flux accuracies in the PACS images are 3% at 70 μm and <5% at 160 μm, with the extended source calibration flux accuracies being uncertain. We also adopt here the more conservative absolute calibration uncertainties of 10% and 20% for integrated source flux densities at 70 and 160 μm, respectively.

For the SPIRE data at 250, 350, and 500 μm, HIPE version 10.0.2751 was used. The data were calibrated and appropriate corrections made to account for several issues, including electrical cross talk, temperature drifts, cosmic-ray hits, "cooler burps," and relative gain factors between bolometers. A naive mapmaker in HIPE was used to produce preliminary images that were destriped. Subsequent iterations of offset fitting and subtraction and destriping were performed until convergence was reached. As in Könyves et al. (2015), the absolute flux accuracy is considered to be <5% for point sources (see Bendo et al. 2013) and <10% for extended sources (see Griffin et al. 2013) in the three SPIRE bands.

Highly smoothed versions of the Herschel images at each wavelength were compared with images made by extrapolating low-resolution data of the same sky locations obtained with the ESA Planck observatory to the Herschel wavelengths after adopting a dust model (Bernard et al. 2010). This comparison allowed appropriate values of the background emission at each wavelength not included in the Herschel data to be determined.

The intensities in all Herschel PACS/SPIRE maps were converted to MJy sr^{-1} and reprojected onto a common grid of $3'' \times 3''$ pixels. Following extensive tests conducted by Könyves et al. (2015) on the HGBS data of Aquila, we expect the absolute astrometric accuracy to be <3". The half-power beam width (HPBW) resolutions of the maps are $8''.4$, $13''.5$, $18''.2$, $24''.9$, and $36''.2$ at 70, 160, 250, 350, and 500 μm, respectively. The pixel sizes of the final images at each wavelength have been set to $3''$, $3''$, $6''$, $10''$, and $14''$, respectively. The HGBS PACS and SPIRE maps of the Cepheus Flare fields data are publicly available on the HGBS Archive (http://gouldbelt-herschel.cea.fr/archives) in standard FITS format. Note that Planck-derived offsets have not been added to these files. Instead, these offsets can be found in the respective header of each map.

3. Results

3.1. Column Densities and Temperatures

Figures 1–5 show H$_2$ column density maps of L1157, L1172, L1228, L1241, and L1251, respectively, obtained by fitting the Herschel spectral energy distributions (SEDs) of each pixel (adding Planck offsets at each wavelength) over a wavelength range of $160-500$ μm with a modified blackbody function. The maps were produced at a resolution of $18''.2$ following the "high-resolution" method described in Appendix A of Palmeirim et al. (2013) that is standard for HGBS catalog papers. The modified blackbody used in the SED fitting includes a dust opacity $\kappa_\nu = 0.144$ cm^2 g^{-1} at 250 μm (incorporating a dust-to-gas ratio of 100) with a power-law dependence with wavelength of index $\beta = 2.0$ (Hildebrand 1983). In addition, the same mean molecular weight per H$_2$ molecule of $\mu = 2.8$ is assumed here (Kauffmann et al. 2008) to convert gas surface density into H$_2$ column density. (To determine the isothermal sound speed, $\mu = 2.33$ is assumed.) Figure 6 shows the dust temperature maps for each field obtained simultaneously from the fitting of modified blackbodies to the multiwavelength Herschel data. In Appendix A, we present the actual Herschel images of each field at 70, 160, 250, 350, and 500 μm in their native resolutions and without the Planck offsets added.

The column densities seen in each map are typical of those seen in other HGBS fields of nearby star-forming molecular clouds, e.g., nonzero column densities are found in every pixel. Similarly, each Cepheus cloud field displays a multitude of substructure on many scales, including compact knots amid longer filaments.

Figure 7 shows histograms of the column densities and temperatures of each field, i.e., their respective probability density functions (PDFs). (Note that the column density PDFs are constructed from all data shown in Figures 1–5 and not only in the last closed contour, as shown recently by Soler 2019.) Table 2 lists the median column density and median temperature of each field shown in Figures 1–6, with associated standard deviations. In terms of column density, L1157, L1172, and L1228 have very similar PDFs, peaking at $(6-7) \times 10^{20}$ cm^{-2} and decreasing to smaller and larger column densities at similar rates. Interestingly, L1241 has column densities that peak at a slightly larger value, about twice that of the others, but its PDF falls off faster at smaller and larger column densities than those of L1157, L1172, and L1228 do. Indeed, the width of L1241's column density PDF is about half that observed in other clouds, and no column densities above 10^{22} cm^{-2} are found. In addition, the column densities of L1251 peak at a similar value to that of L1157, L1172, and L1228, but its PDF falls off slightly more slowly at high column densities. In terms of temperature, all five clouds have distributions that peak at around 14 K. The temperature PDFs of L1157, L1228, and L1251 are similar, with very few pixels with temperatures above 25 K. L1241 has a temperature PDF that is significantly narrower than the others, with few pixels with values above 20 K. In Section 3.2, we report that no protostellar cores are found in L1241. Such objects would otherwise provide internal heating to the cloud, leading to higher temperatures. In contrast, a long tail to 20–40 K is seen in the temperature PDF of L1172. These high temperatures are found in pixels adjacent to the Herbig Ae star HD 200775 (see
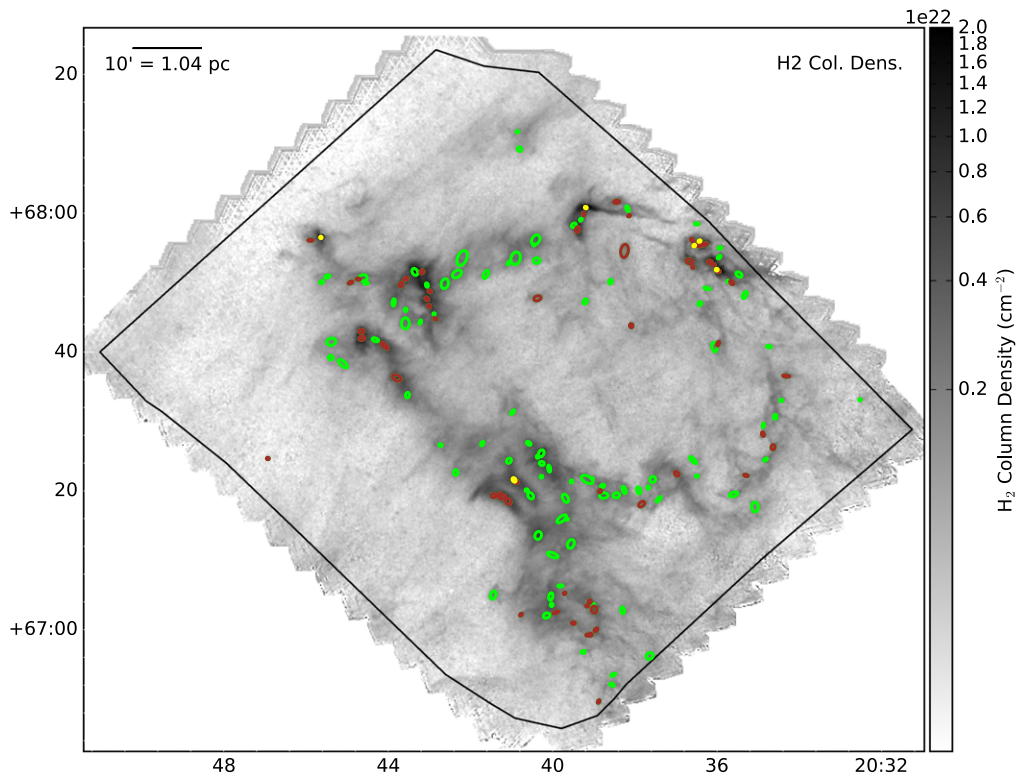
Figure 1. Herschel-derived high-resolution H_2 column densities for L1157. Column densities are shown on a logarithmic scale between 2×10^{21} cm^{-2} and 2×10^{23} cm^{-2}. Ellipses correspond to cores identified in the cloud via *getsources*. Green, red, and yellow ellipses are cores we identify as "starless cores," "candidate prestellar cores," and "protostellar cores," respectively (see Section 3.2). The size of an ellipse corresponds to the measured extent of its respective core. The solid black border excludes noisy map edges and delineates the region in the map over which statistics are calculated.
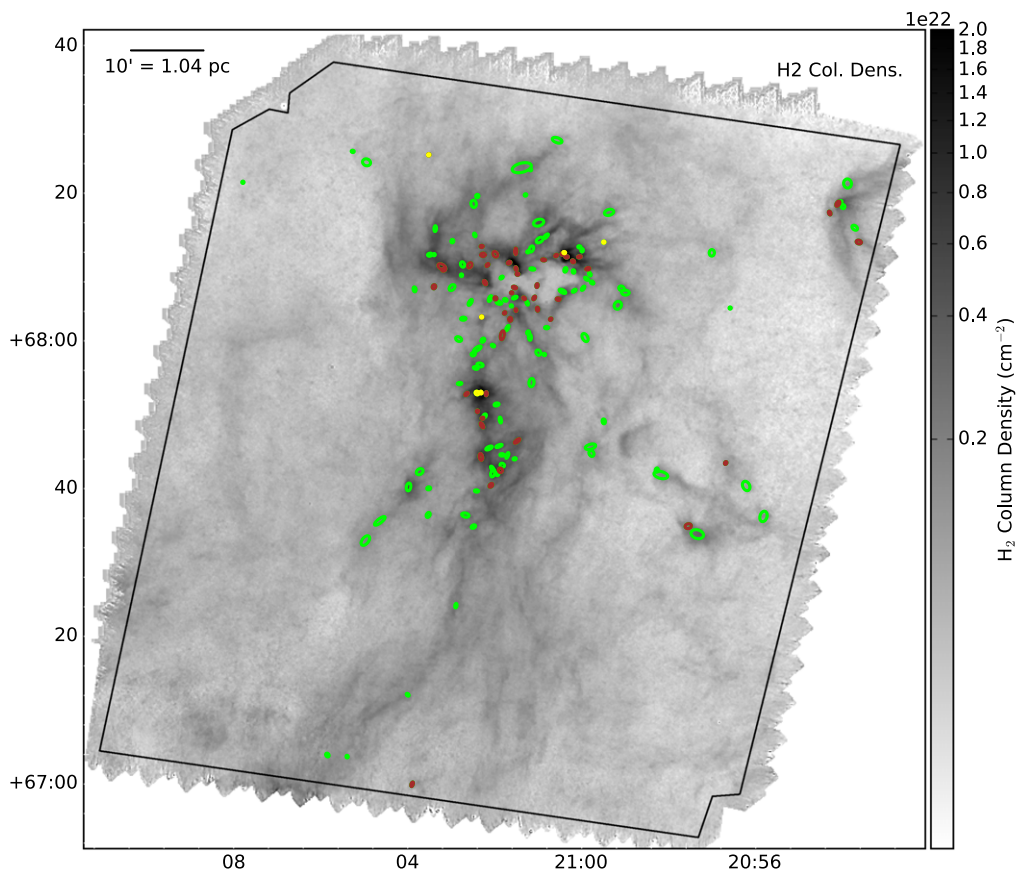
Figure 2. Herschel-derived high-resolution H_2 column densities for L1172. The grayscale range and symbols are defined as for Figure 1.
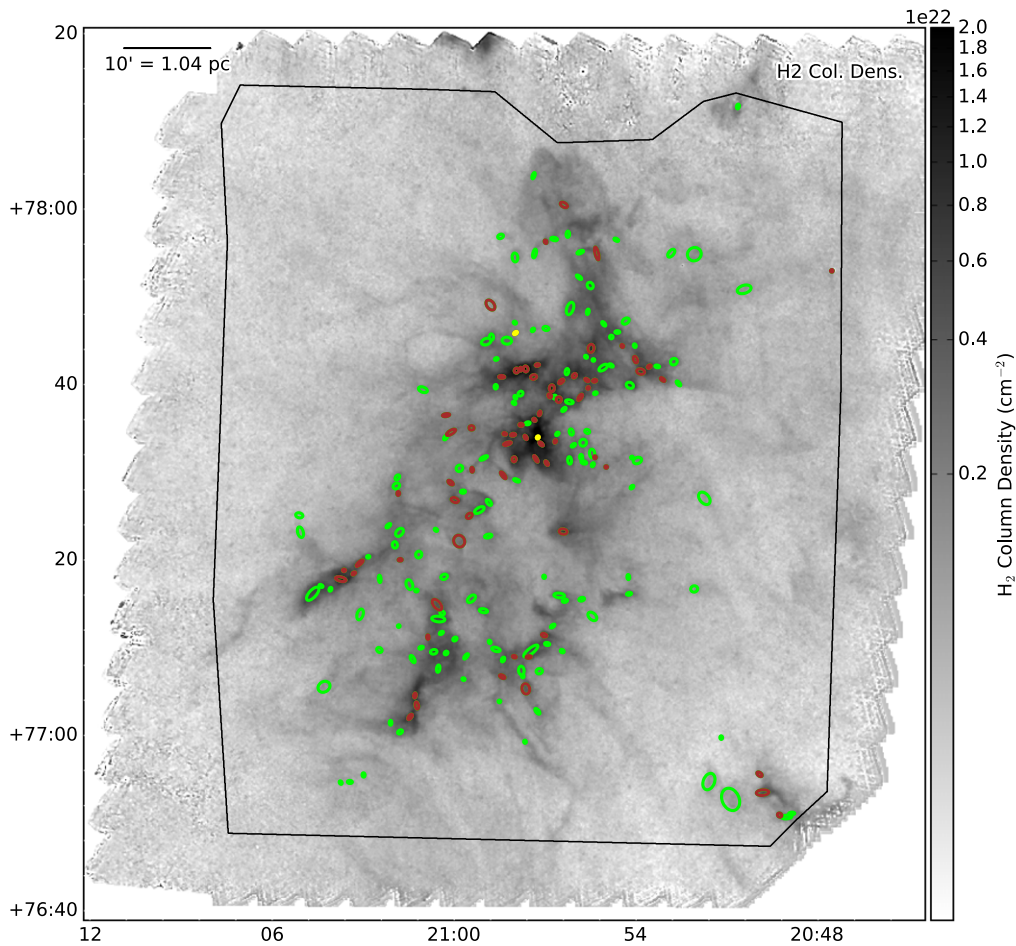
Figure 3. Herschel-derived high-resolution H₂ column densities for L1228. The grayscale range and symbols are defined as for Figure 1.

Figure 6(b)) and hence likely arise from the radiative heating of dust by that particularly luminous star.

Table 3 lists the estimated masses of each Cepheus cloud given the column densities derived here. L1157, L1172, L1228, and L1251 have similar masses of 1400–1900 $M_\odot$, while L1241 is about double that at 3200 $M_\odot$. Table 3 also gives the area of each cloud in pc² given the ∼360 pc distance to the clouds. In addition, Table 3 gives the amount of mass above extinction levels of $A_V = 1$ and 7, where we use the conversion between H₂ column density and extinction of Bohlin et al. (1978). The masses of each cloud at $A_V > 1$ are on average similar (i.e., within 5%–40%) to those reported by Yonekura et al. (1997) from ¹³CO (1–0) observations after adjustment to a distance of 360 pc. From this comparison, we see that L1241 has the largest amount of material at $A_V > 1$ but curiously also the lowest amount of mass (and lowest fraction of total mass) at $A_V > 7$. L1251, however, has the highest amount (and highest fraction) of mass at $A_V > 7$. In total, the Cepheus clouds have ∼500 $M_\odot$ at $A_V > 7$, i.e., ∼8% of the mass of all five clouds at $A_V > 1$.

3.2. Source Extraction

Compact objects in each Cepheus field were extracted using version 1.140127 of the source identification algorithm *getsources* (Men'shchikov et al. 2012). For consistency, this approach is the same as that used to produce other HGBS catalogs of dense cores and protostars (e.g., Könyves et al. 2015). The *getsources* algorithm was specifically developed to identify compact objects

within nonuniform emission across many wavelengths and scales, e.g., in Herschel observations of molecular clouds.

The *getsources* algorithm consists of two distinct "detection" and "measurement" stages. For the first "detection" stage, *getsources* successively smooths input maps to ever lower resolutions, subtracts maps of adjacent resolutions, and identifies positions of significant emission in the difference maps. Comparing these difference maps over many scales and wavelengths (if available) allows sources to be built up and identified over ranges of scale and wavelength. For the second "measurement" stage, *getsources* determines fluxes and sizes of sources using the original input images at each wavelength. Overlapping sources are intelligently deblended. Background levels are subtracted after being determined by linear interpolation under the source footprints, taking into consideration the different native angular resolutions at each wavelength. Finally, *getsources* applies aperture corrections at each wavelength obtained from the SPIRE and PACS Instrument Control Centres (see, e.g., Bendo et al. 2013; Balog et al. 2014, respectively).

We ran *getsources* to extract dense cores and YSOs/ protostars separately in the Cepheus fields, using different input maps and parameters. To extract dense cores, we used the Herschel maps at 160, 250, 350, and 500 μm, regridded to pixels in common, as inputs. These four wavelengths bracket the peak of continuum emission from cold ($T = 10$–20 K) dust in dense cores. We also included the high-resolution column density map (see panel (a) of Figures 1–5) as an additional
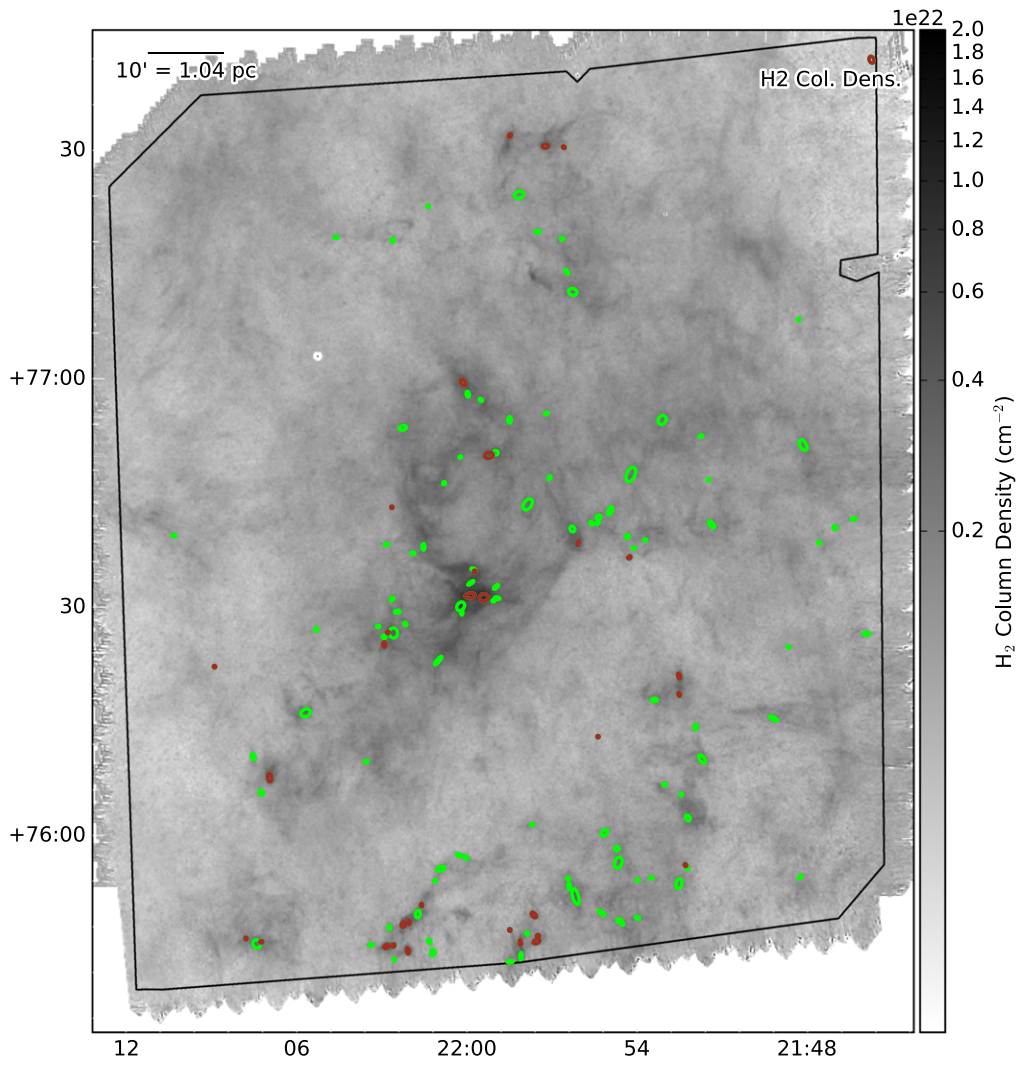
Figure 4. Herschel-derived high-resolution H_2 column densities for L1241. The grayscale range and symbols are defined as for Figure 1.
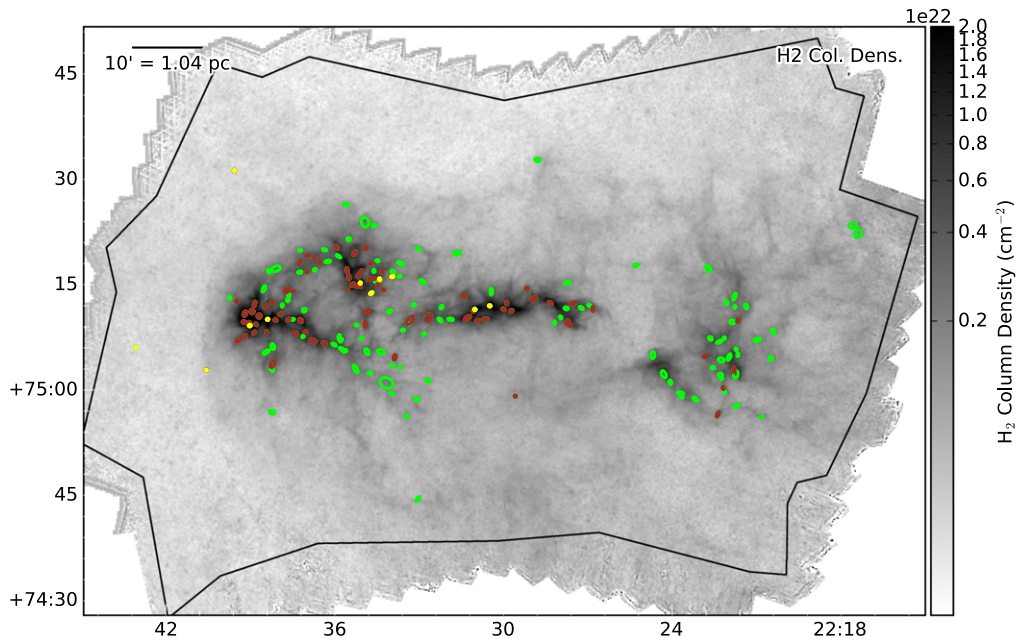

Figure 5. Herschel-derived high-resolution H_2 column densities for L1251. The grayscale range and symbols are defined as for Figure 1.
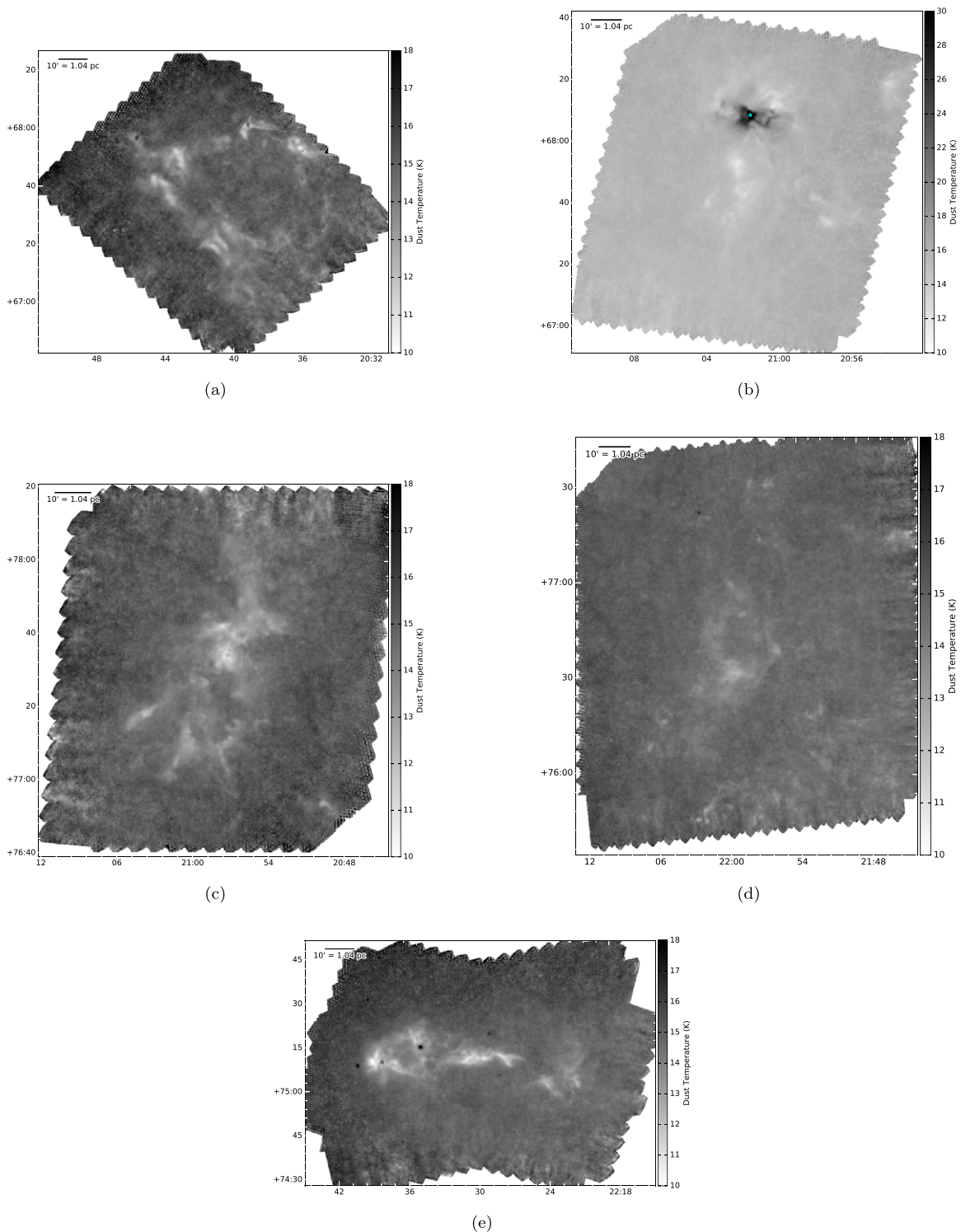
(a)

(b)

(c)

(d)

(e)

Figure 6. Herschel-derived temperatures for (a) L1157, (b) 1172, (c) L1228, (d) L1241, and (e) L1251. The temperatures are shown on a linear scale between 10 and 18 K, except for L1172, which scales linearly between 10 and 30 K. The cyan star shown in panel (b) denotes the position of the Herbig Ae star HD 200775.

"wavelength" input to ensure that identified objects consist of locally high column density. In addition, for the "detection stage" of this extraction, the native 160 μm maps were substituted with ones corrected for anisotropic temperature gradients. These corrected maps were made by converting the native 160 μm maps to pseudo-column-density maps using color temperatures determined from the ratios of the native intensities at 160 and 250 μm, at the latter's resolution. To

extract YSOs or protostars, we used only the Herschel maps at 70 μm. YSOs and protostars will heat their surrounding dust to temperatures higher than those of cold cores, making them stand out obviously at 70 μm as point-like objects (e.g., see Dunham et al. 2008).

For both sets of extractions, source fluxes and sizes are measured from the native Herschel maps of all five wavelengths, appropriately deblended, background subtracted,
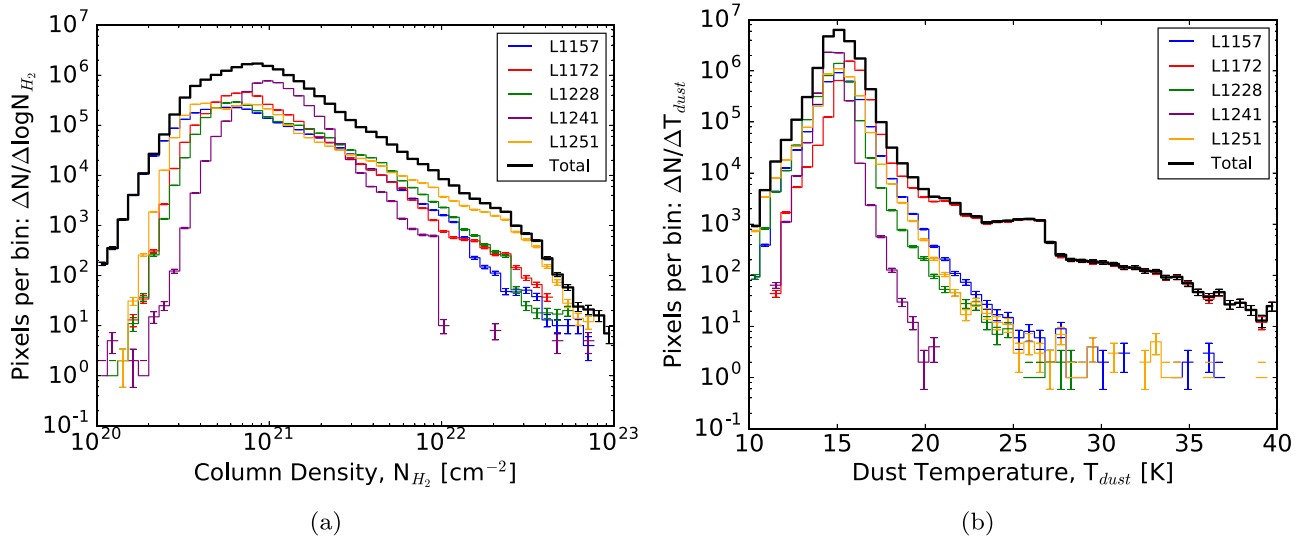
Figure 7. (a) Log-log histogram of Herschel-derived column densities and (b) log-linear histogram of Herschel-derived temperatures for L1157 (blue), L1172 (red), L1228 (green), L1241 (purple), and L1251 (yellow), as well as all five clouds together (black lines).

Table 2
Median and Standard Deviation Values of Column Density and Temperature in Cepheus Flare Clouds

Field	Median Column Density (cm^2)	Standard Deviation of Column Density (cm^2)	Median Temperature (K)	Standard Deviation of Temperature (K)
L1157	6.02E+20	9.60E+20	14.2	0.56
L1172	7.14E+20	9.09E+20	14.7	0.85
L1228	6.37E+20	1.06E+21	14.0	0.33
L1241	9.95E+20	5.40E+20	14.3	0.54
L1251	6.36E+20	1.55E+21	14.3	0.58

Table 3
Mass Distributions of Cepheus Flare Clouds

Cloud	Total Mass $(M_\odot)$	Total Area (pc^2)	Mass at $A_V > 1$ $(M_\odot)$	Mass at $A_V > 7$ $(M_\odot)$
L1157	1400	67	790	66
L1172	1900	91	1000	61
L1228	1600	64	1000	100
L1241	3200	120	2300	10
L1251	1800	77	1100	270
Total	9800	420	6300	510

Table 4
Numbers of Dense Cores (Including Starless Cores, Prestellar Cores, and Protostellar Cores) in the Cepheus Flare Clouds

Field	Dense Cores	Unbound Starless Cores	Candidate Prestellar Cores	Robust Prestellar Cores	Protostellar Cores
L1157	153	86	61	40	6
L1172	156	98	52	31	6
L1228	205	132	71	40	2
L1241	131	98	33	14	0
L1251	187	90	86	53	11
Total	832	504	303	178	25

Note. The locations of unbound starless cores, candidate prestellar cores, and protostellar cores in the Cepheus clouds are shown in green, red, and yellow, respectively, in Figures 1–5. Robust prestellar cores are a subset of candidate prestellar cores.

and aperture corrected. Source lists were constructed from identified sources deemed reliable following separate standard criteria for each extraction. These criteria are listed in Appendix B. Finally, to reduce potential contamination by background galaxies, source positions were cross-checked with the NASA/IPAC Extragalactic Database (NED) and the SIMBAD database. Herschel sources found within 6″ (i.e., approximately half the 13.″5 resolution of Herschel at 160 μm) of a known background galaxy were flagged in the final catalogs. The latter sources are not included as cores in the analysis below.

Finally, each remaining source was visually checked. For inclusion in the final catalogs, a source had to be visible as a peak at its location in the images of at least two Herschel wavelengths and the high-resolution column density map. In total, 115 objects were excluded from the final catalogs as a result of such checks.

Table 4 lists the numbers of dense cores obtained from each Cepheus cloud. In total, we identify 832 dense cores from all five clouds observed, and each cloud has ∼150–200 dense cores. Appendix C describes the online material available for this paper, including a catalog of the observed properties of all Cepheus dense cores extracted from the various maps, such as positions, fluxes, and sizes. Table C1 lists the information provided in this catalog. The online material also includes thumbnail images of each extracted core at each Herschel wavelength and in the high-resolution column density map. Figures C1 and C2 show example thumbnail images of two cores, HGBS_J204306.0+675009 (a robust prestellar core; see Section 3.3 below) and HGBS_J203906.3+680216 (a protostellar core; see Section 3.3 below).

We employed a secondary automated object identification algorithm to provide an independent assessment of the sources

extracted from the Herschel images of the Cepheus clouds via *getsources*. For these assessments, we chose to use the Cardiff Sourcefinding AlgoRithm (CSAR; Kirk et al. 2013), an algorithm that identifies sources in single-wavelength images by following intensities down from maxima in the images until neighboring sources or a noise threshold is met. The CSAR algorithm effectively functions as a conservative variant of the widely used *Clumpfind* algorithm of Williams et al. (1994) in two dimensions. We used CSAR on the high-resolution column density map only (i.e., Figures 1–5). The catalog produced by CSAR was checked against that created by *getsources*, and sources found to be in common (i.e., with peaks located within 6″ of each other) are highlighted as such in the *getsources* catalogs with a flag (see Appendix C and online material). The percentages of objects identified by both algorithms are 54%, 46%, 40%, 60%, and 49% for L1157, L1172, L1228, L1241, and L1251, respectively, values broadly consistent with those obtained in other Gould Belt clouds studied with Herschel, e.g., 45% in Aquila (Könyves et al. 2015). In general, *getsources* can identify fainter objects than CSAR because it incorporates information from multiple wavelengths for its assessments.

3.3. Dense Core Masses and Sizes

For each dense core extracted from the Herschel maps, an SED was constructed using integrated fluxes corrected for immediate background emission (e.g., from a host filament). As with the determinations of column densities and temperatures across each cloud, the dense core SEDs were fit with a modified blackbody model, assuming the same dependencies on κ_ν and β (see Section 3.1) to determine masses ($M_{\rm core}$) and line-of-sight-averaged temperatures ($T_{\rm dust}$), following Herschel GBS standard procedures (Könyves et al. 2015). If a core has more than three bands in which it is significant (i.e., $\mathrm{Sig}_\lambda > 5$, where Sig_λ is the monochromatic significance determined by *getsources*), and if the 350 μm flux is higher than the 500 μm flux, two SED fits were made. In the first fit, the 70 μm flux was included, the errors used were the "detection error" = total core flux/Sig_λ, and the weights of the fitting were 1/(detection error)^2. In the second fit, the 70 μm flux was neglected, the errors used were the "measurement error" determined by *getsources*, and the weights of the fitting were 1/(measurement error)^2. If the mass estimate between both runs varied by less than a factor of two, we used the mass and temperature from the second fit. If the mass estimates differed by more than a factor of two, the mass was calculated from the flux of the longest wavelength of significant flux (i.e., $\mathrm{Sig}_\lambda > 5$), assuming a temperature corresponding to the median core temperature from those cores that passed the fitting test described above. Approximately 45% of cores had mass estimates from the different fits that differed by less than a factor of 2. The median dust temperatures for cores were 11.3, 13.6, 11.9, 11.8, and 11.4 K for L1157, L1172, L1228, L1241, and L1251, respectively.

The observed size of each core was determined as the geometrical average of the FWHMs of its major and minor axes in the high-resolution (18″2) column density map of its host Cepheus cloud (FWHM$^{\rm a}_{N_{\rm H_2}}$ and FWHM$^{\rm b}_{N_{\rm H_2}}$, respectively). This angular size was converted to a physical size ($R^{\rm obs}_{\rm core}$) assuming the ∼360 pc distance to the Cepheus Flare clouds (see Section 1). A deconvolved radius was also determined via $R^{\rm decon}_{\rm core} = (R^{\rm obs\,2}_{\rm core} - \overline{\mathrm{HPBW}_{N_{\rm H_2}}}^2)^{1/2}$, where $\overline{\mathrm{HPBW}_{N_{\rm H_2}}}$ is the

physical size of the 18″2 beam, i.e., 0.032 pc at the ∼360 pc distance of the core.

We use the determined mass and size of each core to obtain estimates of their peak column densities ($N^{\rm peak}_{\rm H_2}$), determined from the peak flux densities at the 36″3 resolution of the 500 μm data (see Appendix C and online material). In addition, we determine the average column densities of each core before and after deconvolution ($N^{\rm ave}_{\rm H_2}$ and $N^{\rm ave,d}_{\rm H_2}$, respectively). Next, we determine "peak" (i.e., from the peak column density value; $n^{\rm peak}_{\rm H_2}$) and average volume densities before and after deconvolution ($n^{\rm ave}_{\rm H_2}$ and $n^{\rm ave,d}_{\rm H_2}$), respectively. The "peak" volume density was determined using the peak column density assuming a Gaussian spherical distribution where $n^\circ = N_\circ/(\sqrt{2\pi}\,\sigma)$ and σ is the standard deviation of the Gaussian distribution.

The online material accompanying this paper includes a catalog of derived physical properties of all Cepheus cores, as described in Appendix C. Table C2 lists the quantities found in this catalog, including mass, size, column density, and volume density estimates.

Figure 8 shows the distribution of $M_{\rm core}$ versus $R^{\rm decon}_{\rm core}$ for the core population of all five Cepheus clouds combined. The cores range in size over ∼0.01–0.2 pc and range in mass over ∼0.02–10 $M_\odot$. There are no significant differences in the ranges of core mass and size between clouds.

Based on the derived mass and deconvolved sizes, we explore the dynamical stability of the Cepheus cores by comparing their physical properties to those of a critical Bonnor–Ebert (BE) sphere (Ebert 1955; Bonnor 1956). For example, the mass of a critical BE sphere is defined as

$$M_{\rm BE,crit} \approx 2.4 R_{\rm BE} c_S^2 / G, \tag{1}$$

where $R_{\rm BE}$ is the BE radius, $c_{\rm s}$ is the isothermal sound speed, and G is the gravitational constant. Here we neglect any nonthermal contributions to the support of the core, e.g., from turbulence. For each core, we estimated $M_{\rm BE}$ assuming $R_{\rm BE} = R^{\rm decon}_{\rm core}$ from the high-resolution column density map and assumed $T = 10$ K. We thus define the mass ratio $\alpha_{\rm BE} = M_{\rm BE,crit}/M_{\rm core}$.

We follow the guidance of Könyves et al. (2015) and use the size-dependent limiting BE mass ratio criterion $\alpha_{\rm BE} \leqslant 5 \times (\mathrm{HPBW}_{N_{\rm H_2}}/\mathrm{FWHM}_{N_{\rm H_2}})^{0.4}$ to estimate the dynamical state of a core. Those cores meeting this criterion are deemed "candidate prestellar cores" (i.e., potentially bound by gravity), and those that do not are considered "starless" (i.e., gravitationally unbound). Figures 1–5 show the locations of these types of cores in each Cepheus cloud. By restricting the criterion to $\alpha_{\rm BE} \leqslant 2$, we further define a subset of candidate prestellar cores we call "robust prestellar cores." Those dense cores deemed to be neither prestellar nor protostellar are considered to be "starless cores." Table 4 lists the numbers of starless cores, candidate prestellar cores, and robust prestellar cores found in each cloud. In total, this comparison reveals 504 starless cores, 303 candidate prestellar cores, and 178 robust prestellar cores in the Cepheus clouds. (Twenty-five cores are identified as being protostellar; see Section 3.4 below.) Figure 8 shows the mass versus size distribution of each starless or prestellar core population in the Cepheus clouds. Figure 8 also shows the expected mass ($M_{\rm core}$) versus size ($R^{\rm decon}_{\rm core}$) relationships for critical isothermal BE spheres at temperatures of 7 and 20 K. All the robust prestellar cores have masses near to or

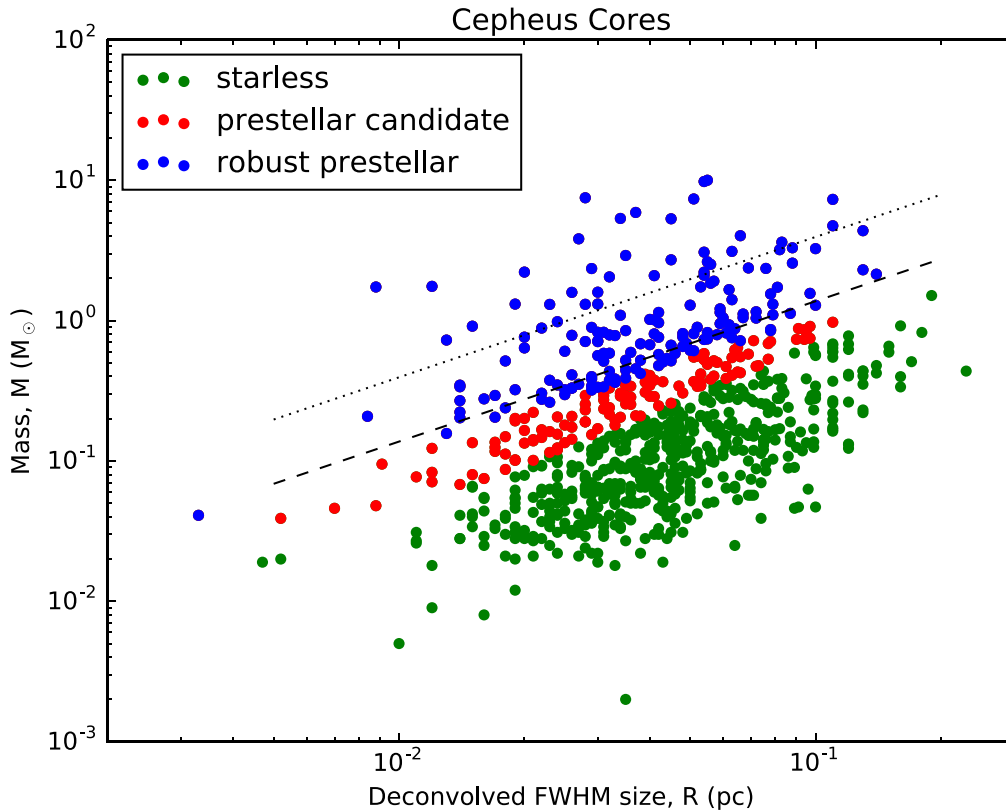**Figure 8.** Mass (M_{core}) vs. deconvolved FWHM size (R_{core}^{decon}) for cores extracted from all five Cepheus clouds. Green, red, and blue circles denote starless cores, candidate prestellar cores, and robust prestellar cores, respectively. Note that robust prestellar cores are a subset of candidate prestellar cores. The critical BE masses for isothermal cores with $T = 7$ and 20 K are shown as black dashed and dotted lines, respectively.

larger than the critical BE mass at a given size and temperature of 7 K.

Könyves et al. (2015) conducted extensive completeness tests of the cores extracted from Herschel maps of the Aquila Rift also via the *getsources* algorithm. They estimated that their sample was 90% complete for cores of observed mass of $0.2\,M_\odot$, assuming an Aquila distance of 260 pc. (From other tests, they determined that observed core masses underestimate the true core mass of dense cores by 20%–30%.) Given the larger distance of the Cepheus clouds of ∼360 pc, we accordingly estimate our 90% completeness as being $0.4\,M_\odot$. Note, however, that Aquila has a lower Galactic latitude ($l \sim 2°–3°$) than the Cepheus clouds ($l \sim 13°–20°$) and thus likely includes more background emission from Galactic cirrus. Hence, we consider our adopted value for Cepheus to be a conservative estimate of our observations' true completeness. Indeed, our completeness estimate of $0.4\,M_\odot$ is largely consistent with those determined for other Gould Belt clouds via modeling similar to that performed by Könyves et al. (2015), after factoring in distance differences (e.g., Benedettini et al. 2018; Ladjelate et al. 2020; Pezzuto et al. 2020).

3.4. Protostellar Cores

Our extractions of sources at 70 μm yield 64 sources across all five Cepheus clouds. The number of 70 μm sources detected in each cloud is 8, 12, 12, 2, and 30 in L1157, L1172, L1228, L1241, and L1251, respectively.

To determine the populations of protostellar cores in the Cepheus clouds, we compare the sources detected at 70 μm to the dense cores detected at 160–500 μm. We classify as

protostellar those dense cores where a 70 μm source is located within its FWHM ellipse. The catalogs provided in the online material list the observed and derived physical properties of the protostellar cores found in the Cepheus clouds studied here. Only 25 protostellar cores are identified over all five clouds, and Figures 1–5 show the locations of the protostellar cores in each cloud. Table 4 lists the numbers of protostellar cores found in each cloud. L1241 has no protostellar cores identified in its midst, consistent with the finding of Kirk et al. (2009) from Spitzer data that L1241 is without YSOs. With 11 protostellar cores, L1251 has the largest number of such cores in the Cepheus clouds, nearly half the identified population, suggesting that it is currently the most active star-forming cloud of the five studied here. See Section 4.2 for discussion of the relative star-forming activity of these clouds.

Given the focus of this paper on the Cepheus clouds' prestellar core population, we do not discuss further the populations of "naked" 70 μm sources or protostellar cores.

3.5. Filamentary Substructure

As with all other clouds observed as part of the HGBS, the Herschel data reveal that the five Cepheus clouds have extensive substructure, much of it filamentary in morphology (see Figures 1–5). In particular, L1157, L1228, and L1251 appear to be dominated by filaments. L1172 and L1241 also exhibit filaments, but the former is dominated by a high column density clump (NGC 7023), and filaments in the latter appear to be more diffuse.

To quantify the locations of filamentary structure in the Cepheus clouds, we used the "getfilaments" option with
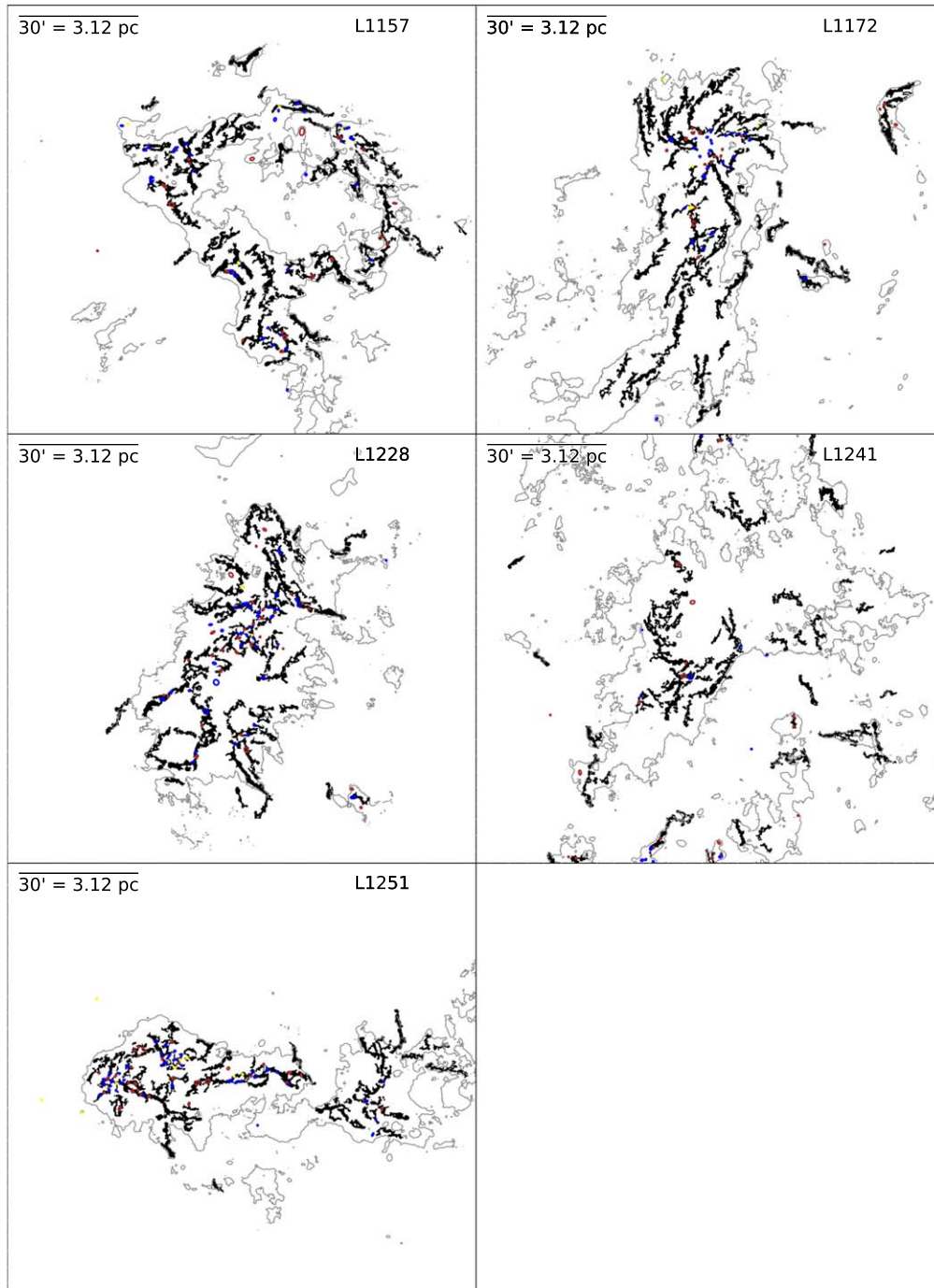
Figure 9. Areas of filaments identified from the H$_2$ column density map derived from Herschel data (dark pixels). Spatial scales up to 0.125 pc (i.e., 72$''$ at 358 pc) are shown. In each field, red, blue, and yellow ellipses indicate the locations and sizes of candidate prestellar cores, robust prestellar cores, and protostellar cores, respectively. For context, the gray contour denotes the 500 μm intensity level of 94.5 mJy beam^{-1}.

standard parameters during our core extractions with *get-sources* (see Men'shchikov 2013). This option provides as output the locations of long contiguous features in input maps that are identified using standard extraction parameters as part of the multiscale processing of those maps by *getsources*. Figure 9 shows the locations of filaments identified in each Cepheus cloud from their respective Herschel-derived H$_2$ column density maps up to spatial scales of 0.125 pc (i.e., 72$''$ at the 358 pc distance to the Cepheus clouds), along with the positions and sizes of associated cores.

Figure 9 illustrates how cores in Cepheus are predominantly located on filaments. Figure 10 shows a histogram of the fractions of cores by type that are coincident with filaments in the Cepheus clouds. For this comparison, a core was considered to be "on filament" if its central pixel overlapped with the area of an identified filament, i.e., the locations identified in Figure 9. Some variation between clouds is seen, with L1241 having cores with the least association with filaments (~40%–50%) and L1251 having almost all its cores (~80%–100%) associated with filaments. Excluding L1241,
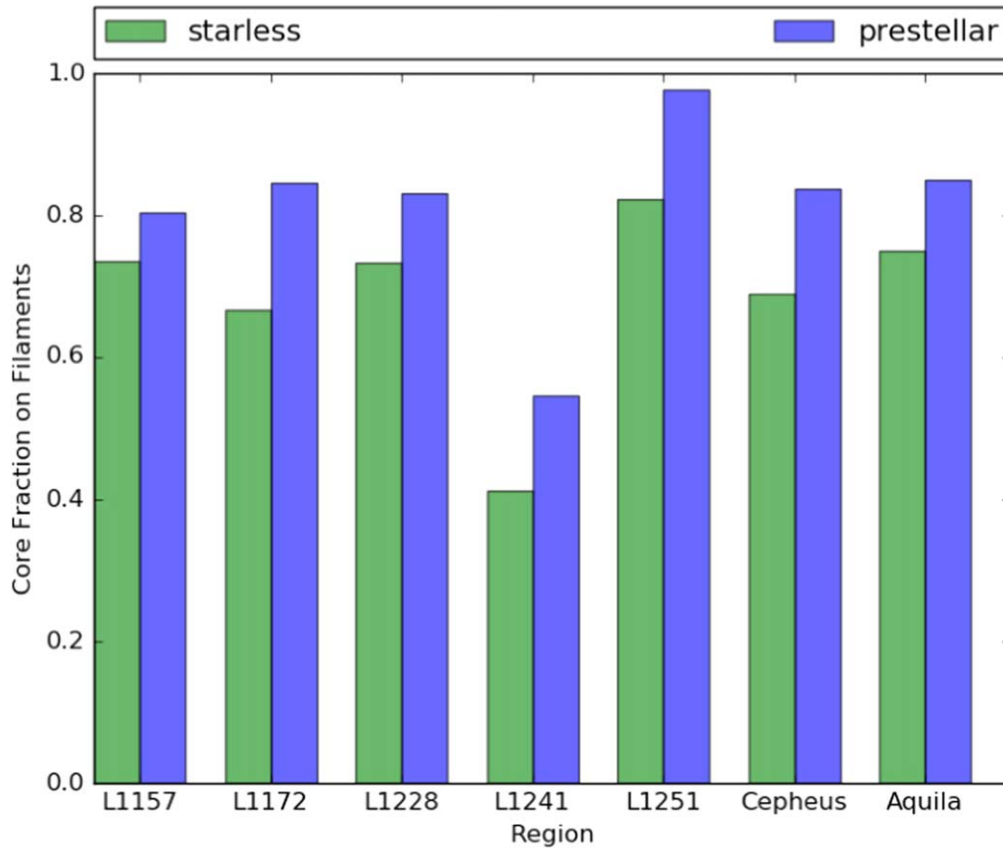
Figure 10. Histogram of percentages of cores found to be coincident with filamentary structure in the Cepheus clouds. Green indicates starless cores, and blue indicates candidate prestellar cores.

~75% of starless cores and ~80% of candidate prestellar cores are coincident with filaments in Cepheus. The percentages of robust prestellar cores on filaments are similar to those of candidate prestellar cores on filaments. These percentages are roughly equivalent to those obtained for other HGBS clouds, e.g., Aquila (see Figure 14 of Könyves et al. 2015).

4. Discussion

4.1. Star Formation in Low Column Density Environments

Though the Cepheus clouds show extensive filamentary substructure and their cores are largely associated with that substructure, the clouds have relatively low column densities. For example, the Cepheus clouds have median H_2 column densities of $\sim(6-10) \times 10^{20} \, cm^{-2}$ (see Table 2), corresponding to extinction levels of $A_V \approx 0.6-1.0$ (Bohlin et al. 1978). For this discussion, we do not subtract foreground/background column densities determined from emission by dust that is arguably unrelated to the cloud. From the histograms of column density in each map shown in Figure 7(a), we surmise that the foreground/background column densities for these clouds are likely on the order of $\sim(1-2) \times 10^{20} \, cm^{-2}$. Since the filament and cores in which we are interested in each cloud typically have column densities an order of magnitude larger than this value or more, we do not correct for systematic increases in their total column densities here.

To put the column densities of the Cepheus clouds into perspective, we note that there has been considerable discussion in recent years about a threshold column density for core formation in filaments of $A_V \approx 7-8$. The physics behind this threshold may be understood from the isothermal infinite cylinder model of Ostriker (1964), which becomes critically stable when its line mass (mass per unit length) $M_{line} = 2c_s^2/G \approx 16 \, M_{\odot} \, pc^{-1}$ at 10 K. Assuming a common filament width of 0.1 pc (see Arzoumanian et al. 2011, 2019), this nominal line mass occurs at $A_V \approx 7-8$ in filaments (André et al. 2014). Indeed, such a threshold appeared evident in the Aquila Rift cloud, where 75% of prestellar cores are associated with filaments with line masses $\geqslant 16 \, M_{\odot} \, pc^{-1}$ (Könyves et al. 2015). More recent works than Ostriker (1964), however, have posited that "transcritical" filaments, i.e., with line masses within a factor of ~ 2 of this critical value (e.g., $8-32 \, M_{\odot} \, pc^{-1}$ at 10 K), are actually those susceptible to fragmentation, leading to less of a sharp threshold and more of a smooth transition for core formation with column density in filaments, as has been observed (Inutsuka & Miyama 1997; Fischera & Martin 2012; Arzoumanian et al. 2019; Könyves et al. 2020).

Only 0.02%–0.9% of pixels in all five Cepheus clouds have column densities $>8 \times 10^{21} \, cm^{-2}$, i.e., $A_V > 8$. Nevertheless, modest star formation is indeed occurring in the Cepheus clouds. Such activity is evident by the 303 candidate prestellar cores and 25 protostellar cores identified in the Herschel data alone (Table 4). Moreover, Kirk et al. (2009), using Spitzer data, find 93 YSO candidates, mostly Class II objects, in L1172, L1228, and L1251. Notably, they find only one YSO candidate in L1241. As mentioned earlier, L1157 was not included in their study.

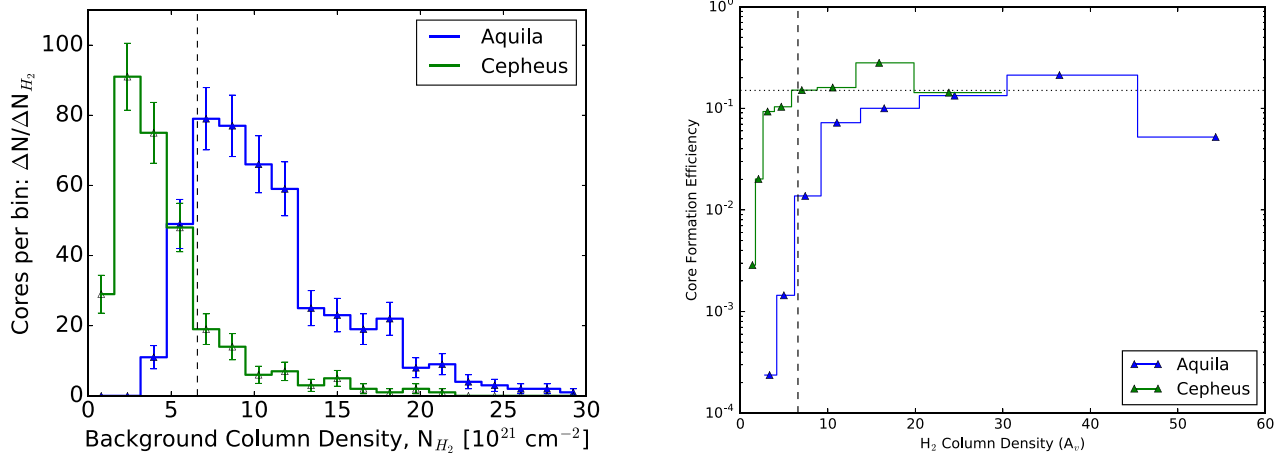In terms of core formation activity, the Cepheus clouds appear similar to other low column density environments

Figure 11. Left panel: histogram of numbers of candidate prestellar cores vs. background H_2 column densities of cores in the Cepheus clouds (green) and the Aquila Rift (blue). Error bars are from Poisson statistics. The dashed line indicates a background column density of $A_V \approx 7$; see Könyves et al. (2015). Right panel: observed differential core formation efficiencies (CFE$_{obs}$) as a function of background column density expressed in units of A_V for the Cepheus clouds (green) and the Aquila Rift (blue).

observed by Herschel, e.g., Lupus I, III, and IV (Benedettini et al. 2015, 2018). In these particular clouds, Benedettini et al. (2015) do find column density PDFs of similar morphology to those of the Cepheus clouds that also peak at $(0.5–1.0) \times 10^{21}$ cm^{-2} (see their Section 3.1). More recently, Benedettini et al. (2018) identify ∼30% fewer numbers of cores in Lupus than what we find over all five Cepheus clouds, e.g., 532 dense cores, of which 102 are candidate prestellar cores. For comparison, the Lupus clouds are ∼160 pc from the Sun (Dzib et al. 2018), less than half the distance to the Cepheus clouds. As with Cepheus, Benedettini et al. (2018) find that almost all Lupus prestellar cores are associated with filaments, though only a third of the Lupus starless cores are so associated. They also find that 90% of Lupus prestellar cores are located in backgrounds of $A_V \geqslant 2$, an extinction level much lower than that seen in other Gould Belt clouds (e.g., Aquila; see Könyves et al. 2015).

Benedettini et al. (2015) find the median column densities of filaments in the Lupus I, III, and IV clouds to be $(1.2–1.9) \times 10^{21}$ cm^{-2}. Relatedly, they find the median line mass of filaments in the Lupus clouds to be ∼3 $M_\odot$ pc^{-1} (see their Figure 15), somewhat lower than the transcritical range of $8–32\, M_\odot$ pc^{-1} for cylinder stability at 10 K (Arzoumanian et al. 2019). Clearly, filaments remain extremely relevant to core (and star) formation, even in instances like Lupus where their median column densities are lower than that range. Given the large degree of correspondence of cores with filaments in Lupus but lower column densities, Benedettini et al. (2015) and Benedettini et al. (2018) suggest that the condition for overdensity needed for filament fragmentation, i.e., within the transcritical range of column densities, may be only reached locally in Lupus filaments. Indeed, observed filaments are not constant column density structures and can exhibit significant variations along their lengths (see, e.g., Roy et al. 2015). Hence, a low average line mass for an entire filament is not a good parameter for determining whether or not stars will form in that filament.

Table 5 lists the median and mean column densities of filaments in the Cepheus clouds (see Figure 9). These values were computed from the column density map using the definitions of filaments shown in Figure 9 and reflect all mass

Table 5
Median and Mean H_2 Column Densities of Filaments in Cepheus Flare Clouds

Field	Median Column Density (cm^{-2})	Mean Column Density (cm^{-2})
L1157	1.9E+21	2.5E+21
L1172	1.8E+21	2.4E+21
L1228	2.3E+21	3.0E+21
L1241	2.0E+21	2.2E+21
L1251	2.7E+21	4.4E+21

traced within those filaments, including cores. The median filament column densities are $(1.8–2.7) \times 10^{21}$ cm^{-2}, about a factor of ∼1.5 higher than the range of those in the Lupus clouds. Adopting an average filamentary width of 0.1 pc (Arzoumanian et al. 2011, 2019), the median Cepheus filament column densities translate into median line masses of $4–6\, M_\odot$ pc^{-1}. The mean column densities of the Cepheus filaments, however, are $(2.2–4.4) \times 10^{21}$ cm^{-2}, which translate into mean line masses of $5–10\, M_\odot$ pc^{-1}, i.e., 25%–66% higher than the median line masses, indicating that the line masses of filaments in these clouds are skewed somewhat above the median, unlike in Lupus. This range of line masses is just below to within the range of transcritical masses at 10 K, i.e., $M_{\mathrm{line}} = 8–32\, M_\odot$ pc^{-1}.

In the left panel of Figure 11, we show the distribution of background column densities for candidate prestellar cores in the Cepheus clouds. The distribution clearly peaks at a column density of $\sim(2–4) \times 10^{21}$ cm^{-2}, similar to the mean column densities of the filaments and much lower than the threshold $A_V \approx 7$ column density. Indeed, ∼80% of candidate prestellar cores in Cepheus are found at background column densities of $A_V \leqslant 7$. For comparison, the left panel of Figure 11 also shows the distribution of background column densities for candidate prestellar cores in the Aquila Rift, where only 20% are found at $A_V \leqslant 7$ (Könyves et al. 2015). Note that a significant tail at the higher ends of the distributions is also seen, i.e., up to $\sim 20 \times 10^{21}$ cm^{-2} in Cepheus. If we assume that these background column densities are indicative of the original filament environments in which the respective cores formed,
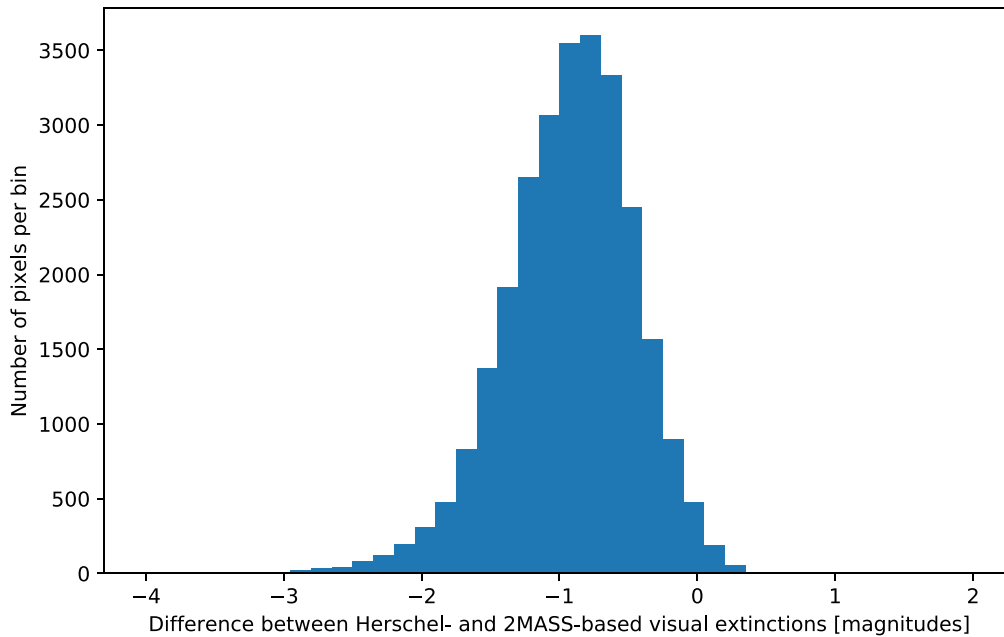
Figure 12. Histogram showing the numbers of pixels in all five Cepheus clouds with differences between extinctions based on Herschel data and those based on 2MASS data. The Herschel-based column densities were first smoothed to the $4'$ FWHM resolution of the 2MASS extinction maps, regridded onto the same $2' \times 2'$ pixels of the 2MASS extinction maps, and converted to A_V using the conversion factor of Bohlin et al. (1978).

then by number $\sim$56% of Cepheus candidate prestellar cores formed in filaments with line masses below the transcritical range and $\sim$44% from filaments with line masses within that range. The original filament line masses, of course, would be larger if the mass we see now in cores was initially distributed more widely within their host filaments. With that possibility in mind, the split is likely on the order of 50–50.

For further comparison, the right panel of Figure 11 shows the observed differential core formation efficiencies ($\mathrm{CFE_{obs}}$) of both the Cepheus clouds and Aquila, where $\mathrm{CFE_{obs}}(A_V) = \Delta M_{\mathrm{cores}}(A_V)/\Delta M_{\mathrm{cloud}}(A_V)$. Here, $\Delta M_{\mathrm{cores}}(A_V)$ is the mass of the prestellar cores within a given bin of background A_V and $\Delta M_{\mathrm{cloud}}(A_V)$ is the cloud mass estimated from the column density map in the same A_V bin. In Aquila, the $\mathrm{CFE_{obs}}$ rises from very low values at low A_V and levels off at $\sim$15% at high A_V, with a transition around $A_V \approx 7$ (Könyves et al. 2015). In Cepheus, however, the $\mathrm{CFE_{obs}}$ rises much more quickly with A_V and levels off to a similar value of $\sim$15% at lower A_V, with a transition at $A_V \approx 3$.

Given the column densities of filaments in the Cepheus clouds, core formation within them is likely proceeding in a manner that bridges the behaviors identified earlier in Lupus and Aquila. Clearly, the strong association between filaments and prestellar cores throughout Cepheus implicates the role of filaments in the core formation process, as elsewhere. In Cepheus filaments with line masses below the transcritical range, though, i.e., $M_{\mathrm{line}} < 8\,M_\odot\,\mathrm{pc}^{-1}$, cores are likely forming more sporadically and only where conditions have allowed localized filament fragmentation, as seen in Lupus. In cases with line masses within (but at the low end of) the transcritical range, i.e., $M_{\mathrm{line}} > 8\,M_\odot\,\mathrm{pc}^{-1}$, however, cores are likely forming more en masse owing to widespread filamentary fragmentation, as seen in Aquila. Following the left panel of Figure 11, roughly half of the cores in Cepheus may have formed in the former way and half in the latter.

Note that for our column density determinations, we use dust opacity values that are standard for the HGBS, i.e., $\kappa_\nu = 0.144\,\mathrm{cm}^{-2}$ at $250\,\mu$m, which assumes a dust-to-gas ratio of 100 and a power-law dependence with wavelength of index $\beta = 2$ (see Section 3.1). Earlier comparisons of HGBS column densities with extinction maps (Benedettini et al. 2015; Könyves et al. 2020; Pezzuto et al. 2020), however, have indicated that such Herschel-based column densities may underestimate the true column densities at lower extinctions, e.g., $A_V < 4$. To explore this possibility for Cepheus, we used near-infrared data from the Two Micron All Sky Survey (2MASS; Skrutskie et al. 2006) to determine extinction maps of each cloud at $4'$ FWHM resolution and compared these extinctions to those expected from Herschel data. Specifically, Figure 12 contains a histogram showing the difference between the extinctions from the two data sets for $A_V < 4$. For this histogram, the $18''$ FHWM resolution Herschel-based column densities were smoothed to the $4'$ FWHM resolution of the 2MASS extinction maps, regridded to the same $2' \times 2'$ pixels of the 2MASS extinction maps, and converted to extinctions using the common A_V-to-H_2 conversion factor of $N(H_2) = A_V \times 0.94 \times 10^{21}$ from Bohlin et al. (1978). The comparison clearly shows that the Herschel data consistently produce lower extinctions than those expected from 2MASS data by $\sim$0–2 mag, with a peak difference at $\sim$1 mag. Though the intrinsic resolutions of the data sets differ significantly, the Herschel-based column density estimates we use as the basis of our discussion here may be systematically lower by $\sim$1 $\times$ $10^{21}\,\mathrm{cm}^{-2}$. Accordingly, the line masses of Cepheus filaments may be systematically larger by $\sim$2 $M_\odot\,\mathrm{pc}^{-1}$, somewhat increasing the fraction of such filaments in the transcritical line mass range. See Benedettini et al. (2015) and Könyves et al. (2020) for discussions of possible sources of the disparity between extinctions and Herschel-derived column densities.

Even with a modest increase in local column densities, star formation is occurring in Cepheus in relatively low column density environments. Cores have likely formed in relatively low numbers in Cepheus owing to its significant number of lower column density filaments, relative to clouds widely containing filaments at higher (i.e., critical) column densities.
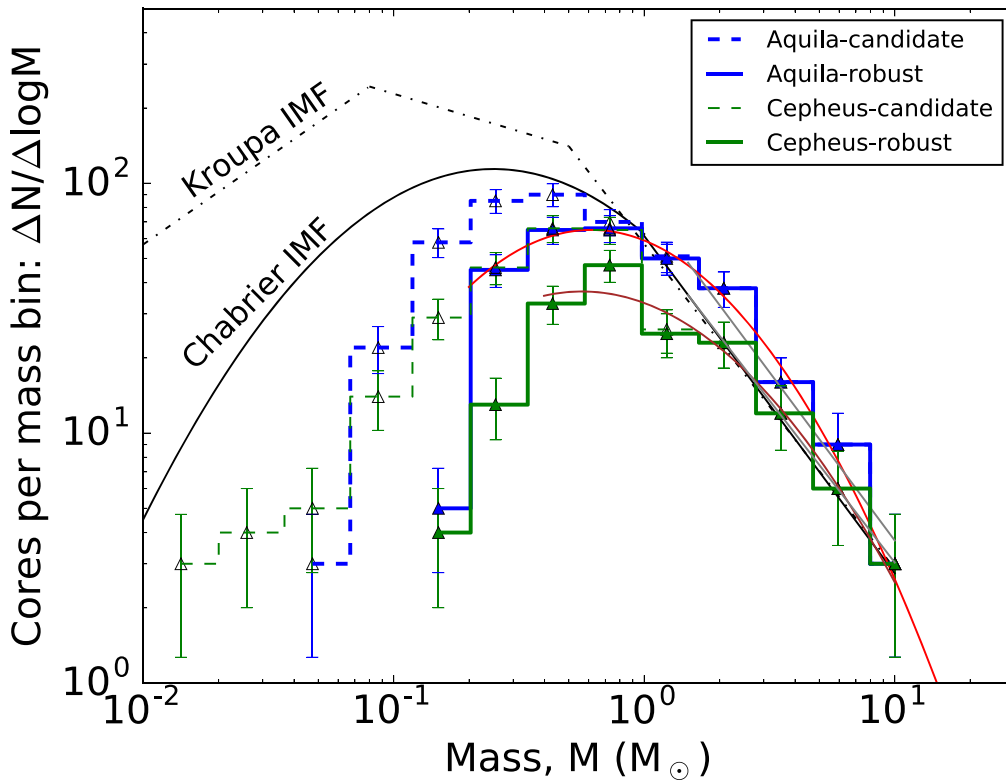
Figure 13. Mass functions of candidate prestellar (dashed histograms) and robust prestellar (solid histograms) cores in the Cepheus clouds (green) and the Aquila Rift (blue). The numbers of candidate and robust prestellar cores in each sample are 303 and 187 (Cepheus) and 446 and 292 (Aquila), respectively. Error bars are from Poisson statistics. The brown and red lines indicate lognormal fits to the Cepheus and Aquila robust prestellar mass functions, respectively, excluding the lowest-mass bins, which are likely incomplete. The lognormal fits have peaks at 0.56 and 0.62 $M_\odot$ and standard deviations of 0.54 and 0.48, respectively. For comparison, the black solid and dashed–dotted lines show the stellar IMFs of Chabrier (2005) and Kroupa (2001), respectively, after scaling by a factor of 10^3.

Namely, with widespread fragmentation being less available in lower column density filaments, relatively fewer cores would be expected to be produced per filament. Though the range of mean column density in the Cepheus clouds is narrow, it is notable that the numbers of candidate and robust prestellar cores in each cloud roughly track monotonically (though less than linearly) with the mean column density of the filaments in each cloud, with the lowest numbers of prestellar cores found in L1241 and the highest in L1251 (see Tables 4 and 5). In addition, the numbers of Cepheus candidate prestellar cores show that roughly half at present have formed in lower column density filaments (see Figure 11, left panel). The low number of prestellar cores likely has had a concomitant effect on the productivity of star formation in Cepheus and likely accounts for these clouds' relatively modest protostellar yields. Indeed, the relative unavailability of transcritical filaments widely in lower column density clouds may simply explain why such clouds do not form as many cores and stars as clouds with higher column densities do.

4.2. Core Mass Functions

Figure 13 shows the number distributions of candidate and robust prestellar core mass in Cepheus. The two core mass functions (CMFs) are virtually the same at the high-mass end, i.e., $M_{obs} \geqslant 1\,M_\odot$. Both CMFs peak at $\sim 0.7\,M_\odot$, but the robust prestellar CMF falls off more quickly to lower masses than the candidate prestellar CMF does, likely because it is more difficult for lower-mass cores to satisfy the requirement that a robust prestellar core have $\alpha_{BE} \leqslant 2$ (see Section 3.3). Indeed, the cores of the robust prestellar CMF are arguably

those most likely to collapse imminently to form a new generation of stars. Notably, we find no robust prestellar cores in Cepheus of mass below $0.1\,M_\odot$, but a few candidate prestellar cores of mass $< 0.1\,M_\odot$ are seen. These scarcities of low-mass prestellar cores are likely related to our expectation that our source extractions are 90% complete to cores of mass $\approx 0.4\,M_\odot$. Note, however, that the peaks of the prestellar CMFs are well above the 90% completeness limit, indicating that they have not been artificially induced owing to incompleteness. As found in other clouds studied in the HGBS, the robust prestellar CMF in Cepheus shows an overall lognormal shape. Indeed, a lognormal fit to that CMF, performed with Levenberg −Marquardt least-squares minimization over bins at and above the $0.4\,M_\odot$ mass limit of 90% completeness, has a peak at $0.56 \pm 0.21\,M_\odot$ and a width $\sigma = 0.54 \pm 0.06$ dex. We note that these errors are likely lower limits since we do not consider uncertainties in the masses of individual cores when fitting these CMFs.

Figure 13 also shows the candidate and robust prestellar CMFs for the Aquila Rift, as found by Könyves et al. (2015) using a distance[15] of 260 pc. The robust prestellar CMFs of Cepheus and Aquila show two important similarities and one difference. The first similarity is in the widths of

---

[15] Based on GAIA data, Ortiz-León et al. (2018) have recently suggested an Aquila distance of 436 ± 9 pc, which would shift the Aquila CMFs upward in mass by a factor of ~ 2.8 but not change significantly their prestellar core memberships or lognormal shapes. We have retained the earlier distance for this discussion, as it is unclear how much of Aquila corresponds to 436 pc (see Palmeirim et al. 2020, in preparation). We note that the ultimate conclusions of this paper do not depend on the distance to Aquila.
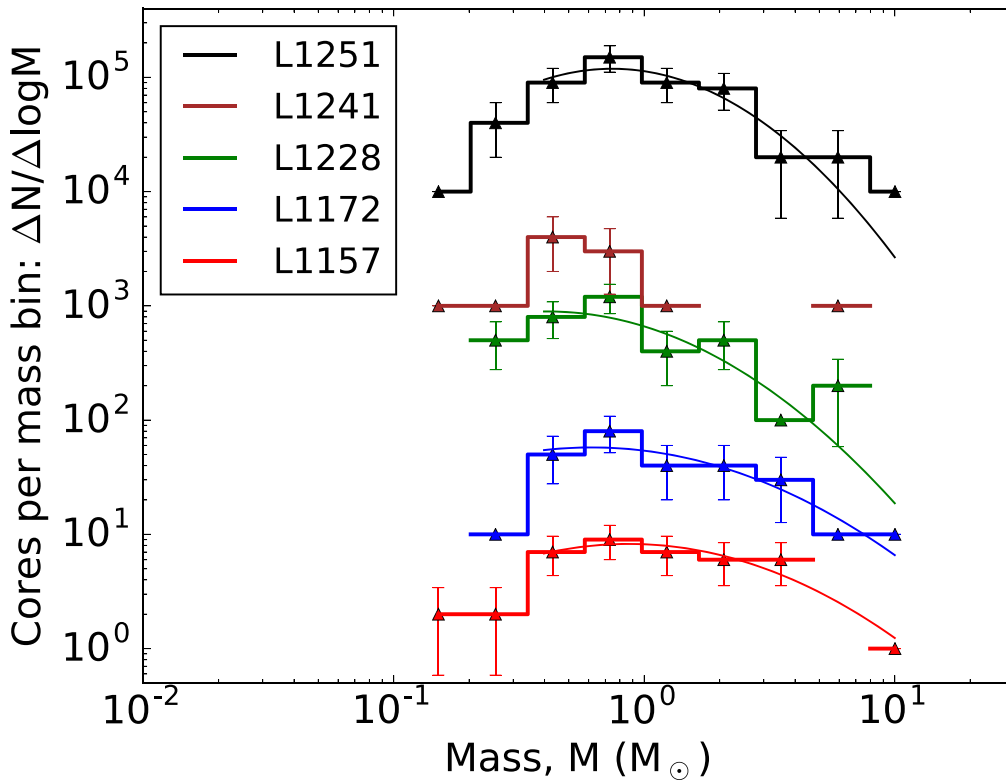
Figure 14. Mass functions of robust prestellar cores in each Cepheus cloud: L1157 (red), L1172 (blue), L1228 (green), L1241 (brown), and L1251 (black). Error bars are from Poisson statistics. To allow easier comparison of the cloud CMFs, the values for the last four clouds have been artificially shifted up by multiplying each successively by an increasing order of magnitude. Lognormal fits to L1157, L1172, L1228, and L1251 at $M \geqslant 0.4\,M_\odot$ are also shown. Note that the L1241 mass function was unable to be fit by a lognormal.

lognormal fits to the two robust prestellar CMFs, e.g., 0.54 ± 0.06 dex for Cepheus versus 0.48 ± 0.02 dex for Aquila. The second similarity is in the peaks of these CMFs, e.g., $0.56\,M_\odot \pm 0.21\,M_\odot$ for Cepheus versus $0.62\,M_\odot \pm 0.04\,M_\odot$ for Aquila. The difference, however, is between the heights of the clouds' CMFs, which can be simply attributed to the fact that Cepheus has $\sim$60% as many robust prestellar cores as Aquila, e.g., 178 versus 292, respectively. Nevertheless, this comparison reveals that the lognormal fits to the robust prestellar CMFs in both clouds are very similar. Note that the 90% completeness core mass limit for Cepheus ($0.4\,M_\odot$) is roughly twice that of Aquila ($0.2\,M_\odot$).

For further comparison, Figure 13 also shows the stellar initial mass functions (IMFs) determined by Kroupa (2001) for single stars and by Chabrier (2005) for multiple systems. These IMFs have each been scaled by a factor of 10^3 so they can be plotted alongside the CMFs. Both IMFs are also lognormal in character, though they peak at much lower masses than the Cepheus and Aquila CMFs. The 0.54 ± 0.06 dex width of Cepheus's robust prestellar CMF is remarkably similar to the 0.55 dex width of the Chabrier IMF of Galactic disk stellar systems (Chabrier 2005), but it is narrower than the Kroupa IMF of single stars. Indeed, comparing the peaks of the Cepheus robust prestellar CMF and the Chabrier IMF, an efficiency factor of $\epsilon \approx 0.3$–0.4 is implicated, similar to the $\epsilon \approx 0.4$ estimated from the Aquila CMF by Könyves et al. (2015). (Of course, this picture assumes that the efficiency factor is constant over a wide range of mass.) At their higher-mass ends, the slopes of both the Cepheus and Aquila CMFs are also consistent with each other within uncertainties, i.e., -1.31 ± 0.01 and -1.35 ± 0.14, respectively. In turn, these

values are themselves consistent with the -1.35 slope of the high-mass end of the IMF determined by Salpeter (1955).

Figure 13 shows the CMF compiled from all five Cepheus clouds, including 178 robust prestellar cores. To explore deeper into the makeup of the lognormal CMF, it is instructive to examine such CMFs drawn from the individual Cepheus clouds. Accordingly, Figure 14 shows the robust prestellar CMFs from each Cepheus cloud, assembled from populations of 14 (L1241) to 53 (L1251) prestellar cores each (see Table 4). (Note that the CMFs in Figure 13 have been shifted vertically by multiples of orders of magnitude so their shapes can be more easily compared.) Some variation between the shapes of the individual cloud CMFs is seen. The CMFs of L1172 and L1251 appear the most lognormal-like, but those of L1228 and L1241 look remarkably flat. With five central bins of similar height, the peak of L1157's CMF is hard to define, and so this CMF seems somewhere in between a lognormal and flat distribution. Of course, the smaller numbers of cores per bin in each cloud's CMFs make it hard to tell by eye if the distributions differ significantly.

To provide a quantitative sense of the morphologies of the robust prestellar CMFs of each cloud, we fit lognormals to each CMF at and above $0.4\,M_\odot$, the 90% completeness core mass limit. Table 6 shows the results of the peak mass and width of the lognormal fit to each cloud's robust prestellar CMF with uncertainties. The results for the combined robust prestellar CMF for all five Cepheus clouds are also listed. A lognormal fit is not possible for L1241, especially given the $0.4\,M_\odot$ lower limit restricting the sample available to fit. Also, the lognormal fit for L1228 is rather poor, as evidenced by the large uncertainties in peak mass and width listed in Table 6.

Table 6
Results of Lognormal Fits to Individual Cepheus Cloud Robust Prestellar
CMFs at $M \geqslant 0.4\,M_{\odot}$

Field	Lognormal Peak Mass ($M_{\odot}$)	Lognormal Width (dex)
L1157	0.87 ± 0.21	0.55 ± 0.08
L1172	0.62 ± 0.35	0.58 ± 0.16
L1228	0.41 ± 0.65	0.50 ± 0.30
L1241	...	...
L1251	0.75 ± 0.19	0.41 ± 0.09
Cepheus	0.56 ± 0.21	0.54 ± 0.06

Meanwhile, the peak masses of the robust prestellar CMFs from the three clouds with reasonable lognormal fits show some possible variation but are largely consistent within errors with $0.6\,M_{\odot}$, a little higher than but within errors of the peak mass of the combined CMF. (The peak mass of the combined CMF is slightly lower than the peak masses of the CMFs of L1157, L1172, and L1251 owing to L1228 and L1241 adding mostly lower-mass cores to the ensemble.) Furthermore, the widths of the three CMFs vary between 0.41 and 0.58 dex, but are largely consistent within 1σ of the 0.54 dex width of the combined CMF and the 0.55 dex width of the Chabrier system IMF.

A visual comparison of the individual column density and temperature maps of the Cepheus clouds (see Figures 1–5, 6) shows apparent differences between them, with their characters ranging from more diffuse (L1241) to highly filamentary (L1251) to cluster dominated (L1172). To place these differences in context, recall that the Cepheus clouds are distributed quite widely on the sky. Though they share a common name, the Cepheus clouds are more of a loose association rather than a complex. Hence, it is likely that each is at its own stage and ability in producing stars, one related to its total mass, its fraction of dense gas, its immediate physical environment, and time. With these differences, however, it is perhaps not surprising that the individual cloud CMFs shown in Figure 14 differ in appearance, though the small sample sizes make it difficult to be sure. Nevertheless, the Cepheus clouds are broadly similar in terms of their column density and temperature distributions (see Figure 7), which may explain the broad similarity of the lognormal fits to the CMFs of at least three of the clouds. The combination of all five cloud CMFs, however, into a single CMF that is similar in peak mass and width to those seen elsewhere (e.g., in Aquila) is a remarkable demonstration of how the lognormal core mass function arises out of a wide range of initial conditions.

The common peak and width of the robust prestellar CMFs of various nearby clouds may speak to commonalities in how their cores (and stars) formed. Namely, filaments are seen to be central to developing prestellar cores in clouds. Such filaments likely have a turbulent origin, as bulk motions within clouds drive gas together to form sheets and filaments. Indeed, sheets likely fragment very easily into filaments; see André et al. (2014). Given their turbulent origins, the filaments themselves likely retain density perturbations along their lengths consistent with that turbulence. For example, Roy et al. (2015) noted a potential link between the density fluctuations seeded by turbulence in filaments and the CMF. Hence, the similar peaks and widths of robust prestellar CMFs seen in different clouds could be itself an expression of the common influence of turbulence forming filaments and seeding their density fluctuations. As a result, the system IMF arises from molecular clouds where multiple lognormal populations of robust prestellar cores inefficiently produce stars.

More star-forming clouds than just Cepheus and Aquila need to be examined to see whether the morphological differences and similarities of CMFs noted here are found elsewhere (see, e.g., Fiorellino et al. 2020). Furthermore, it is important to retain the perspective that the Cepheus clouds (and even Aquila), with relatively modest star formation activity, are relatively minor contributors to the total amount of star formation in the Galaxy. Indeed, the IMF would be set by the much larger engines of star formation in the Galaxy, i.e., Giant Molecular Clouds. Therefore, future detailed examinations of the CMFs in those clouds are also necessary.

5. Summary and Conclusions

In this paper, we examined the SPIRE and PACS observations of five Cepheus Flare clouds, L1157, L1172, L1228, L1241, and L1251, that were obtained as part of the Herschel Gould Belt Survey key project. We summarize our main findings below.

1. The Cepheus clouds are relatively low mass clouds of the Gould Belt. Given the column densities obtained from the Herschel data, we estimate their masses to range from $800\,M_{\odot}$ (L1157) to $2300\,M_{\odot}$ (L1241). Like other Gould Belt clouds observed by Herschel, the Cepheus clouds exhibit significant filamentary substructure. The character of the substructure does appear to vary from cloud to cloud, from relatively diffuse (L1241) to more pronounced (L1251) to cluster dominated (L1172).

2. The column density PDFs obtained from the Herschel observations are generally similar, peaking around $1 \times 10^{21}\,\mathrm{cm}^{-2}$ with a power-law-like decline to higher column densities. The column density PDF of L1241, however, is noticeably narrower than the others. The temperature PDFs of all five clouds show similar peaks around 14 K. Those of L1157, L1228, and L1251 have similar widths, while those of L1241 and L1172 are narrower and wider, respectively. These differences are likely due to the absence and presence of significant internal heating sources (i.e,. protostars) in the latter clouds, respectively.

3. Using the *getsources* automated source identification algorithm, we identify 832 dense cores in the Herschel 160–500 μm data. Of the dense cores, 504 are classified as starless (i.e., gravitationally unbound) and 303 are classified as prestellar core candidates from their locations in a mass versus size diagram. A subset of 178 cores from the latter are considered "robust" prestellar cores. The remaining 25 dense cores were found to be coincident with sources extracted independently from the 70 μm data alone and are classified as protostellar cores.

4. The *getsources* algorithm also identified filamentary structure in each Cepheus cloud. With some variation between clouds, ∼75% of starless cores and ∼80% of prestellar cores are found to be coincident with filaments. L1251 has the highest percentages of cores coincident

with filaments (80%–100%), while L1241 has the lowest (40%–60%).

5. The distribution of the background column densities of the population of prestellar cores in the Cepheus clouds peaks at $(2-4) \times 10^{21} \, \mathrm{cm}^{-2}$ but has a small tail leading up to background column densities of $\sim 20 \times 10^{21} \, \mathrm{cm}^{-2}$. Approximately half of Cepheus's candidate prestellar cores appear to have formed in filaments with line masses within but at the lower end of the "transcritical" range at $T = 10$ K, i.e., $M_{\mathrm{line}} = 8–32 \, M_{\odot} \, \mathrm{pc}^{-1}$, and half in filaments with line masses lower than that range. (Further investigation of the opacity values to use at lower extinctions is needed.) In the former case, greater numbers of cores are expected from widespread filament fragmentation, while fewer are expected in the latter owing to fragmentation only occurring where localized conditions warrant. As a result, Cepheus is forming fewer cores than higher column density clouds like Aquila.

6. The mass function of robust prestellar cores (CMF) in all five Cepheus clouds combined is lognormal in shape, with a peak mass of $0.56 \, M_{\odot}$ and a width of 0.54 dex. In comparison, the Aquila Rift CMF has a lognormal shape as well, with a similar peak mass of $0.62 \, M_{\odot}$ and a similar width of 0.48 dex. The Cepheus CMF is consistent with the system IMF of Chabrier (2005), assuming a mass-independent efficiency factor $\epsilon = 0.3–0.4$.

7. The robust prestellar CMFs of L1157, L1172, and L1251 can be also fit by lognormals with peak masses consistent within errors with $\sim 0.6 \, M_{\odot}$ and widths broadly consistent with the 0.55 dex width of the system IMF of Chabrier (2005). The flatter CMFs of L1228 and L1241, however, were unable to be reliably fit with lognormals.

Though filamentary substructure is ubiquitous in the Cepheus clouds, this substructure has mean column densities largely below or at the low end of the range of "transcritical" values associated with the radial cylindrical fragmentation mechanism enabling core formation in filaments. Core formation and evolution in Cepheus appear to bridge that observed in lower and higher column density clouds, such as Lupus and Aquila, respectively. As a result, both localized fragmentation, where conditions permit, and more widespread core fragmentation in transcritical filaments are occurring, producing cores of seemingly equal number. The CMFs of the individual Cepheus clouds reflect their current core formation potential, but in aggregate they reflect a more generalized distribution of prestellar core origins by encompassing a range of environments. Indeed, the common width of the aggregate Cepheus CMF and the Aquila CMF of ~ 0.5 dex hints at a common origin, perhaps due to seeding of the fluctuations that evolve into cores by turbulence. Assuming a mass-independent factor for inefficiently converting core mass into stars, the system IMF may originate from CMFs of similar width from numerous clouds.

Appendix A
Herschel Observations of Cepheus Clouds

In Figures 15−19, we provide the Herschel images of L1157, L1172, L1228, L1241, and L1251 at 70, 160, 250, 350, and 500 μm, respectively, at their native resolutions and without the respective Planck offsets added.
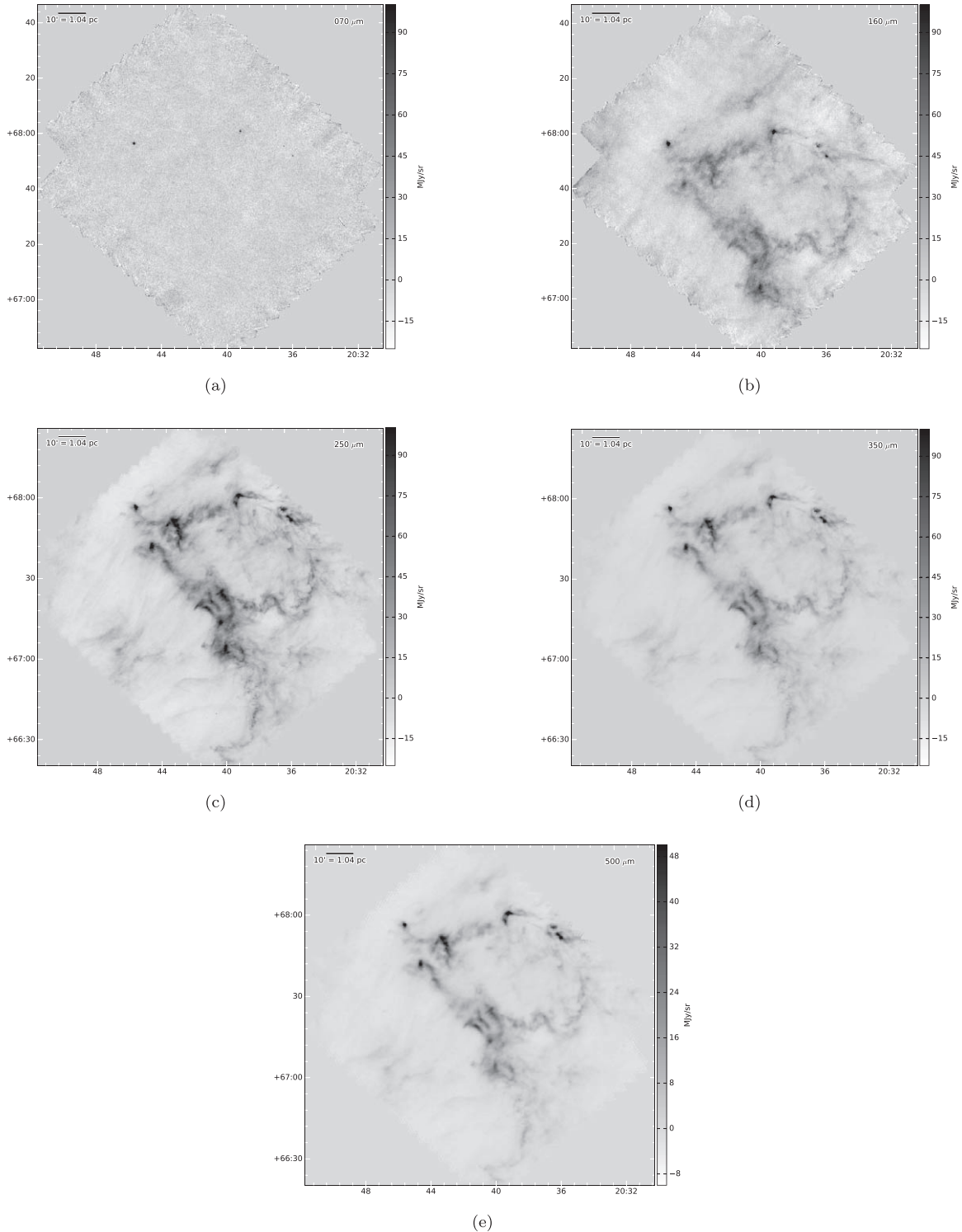

Figure 15. Herschel observations of L1157 at (a) 70 μm, −25 to 100 MJy sr^{-1}; (b) 160 μm, −25 to 100 MJy sr^{-1}; (c) 160 μm, −25 to 100 MJy sr^{-1}; (d) 350 μm, −25 to 100 MJy sr^{-1}; and (e) 500 μm, −10 to 50 MJy sr^{-1}.
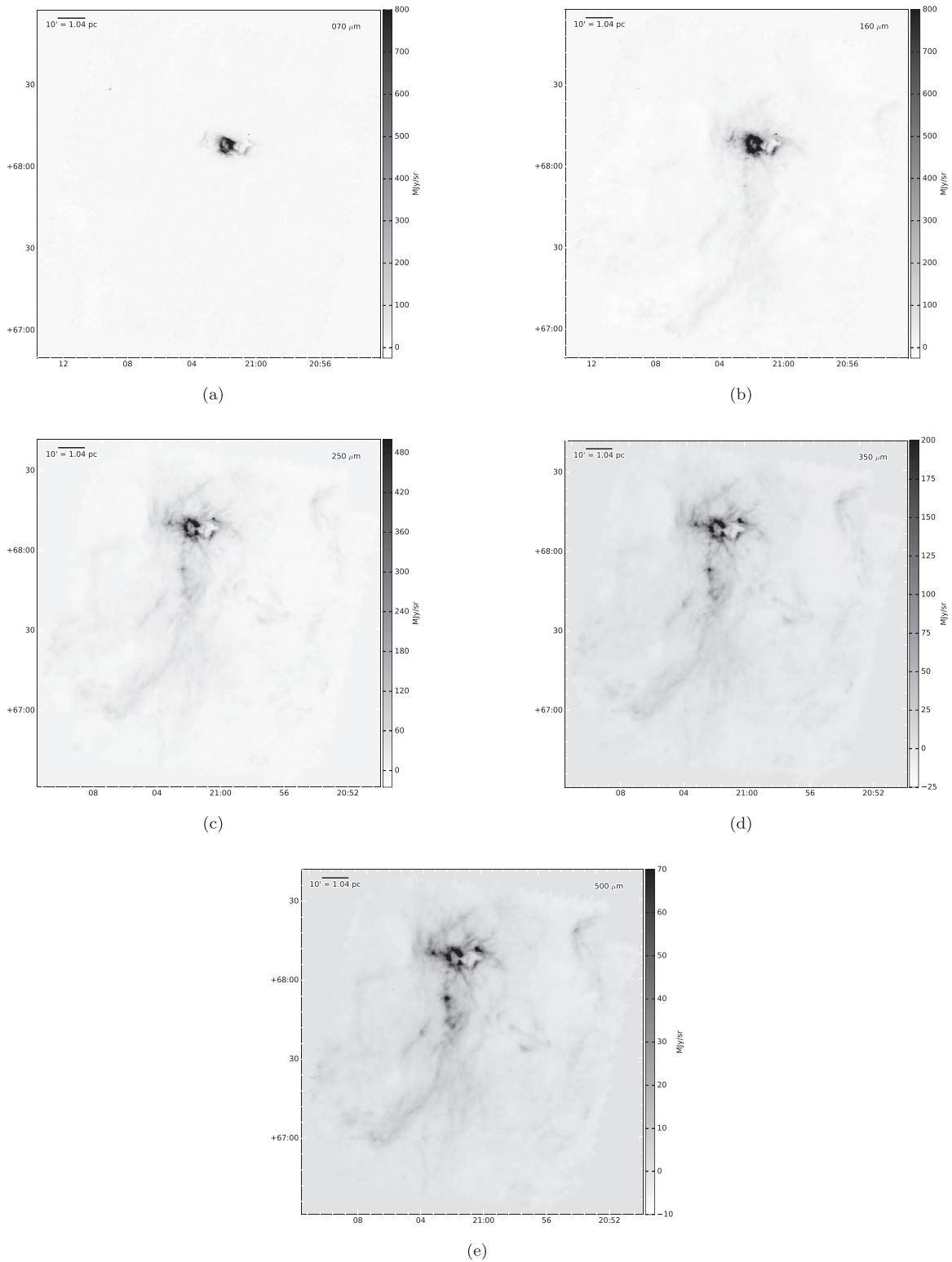
Figure 16. Herschel observations of L1172 at (a) 70 μm, -25 to 100 MJy sr^{-1}; (b) 160 μm, -25 to 100 MJy sr^{-1}; (c) 160 μm, -25 to 100 MJy sr^{-1}; (d) 350 μm, -25 to 100 MJy sr^{-1}; and (e) 500 μm, -10 to 50 MJy sr^{-1}.
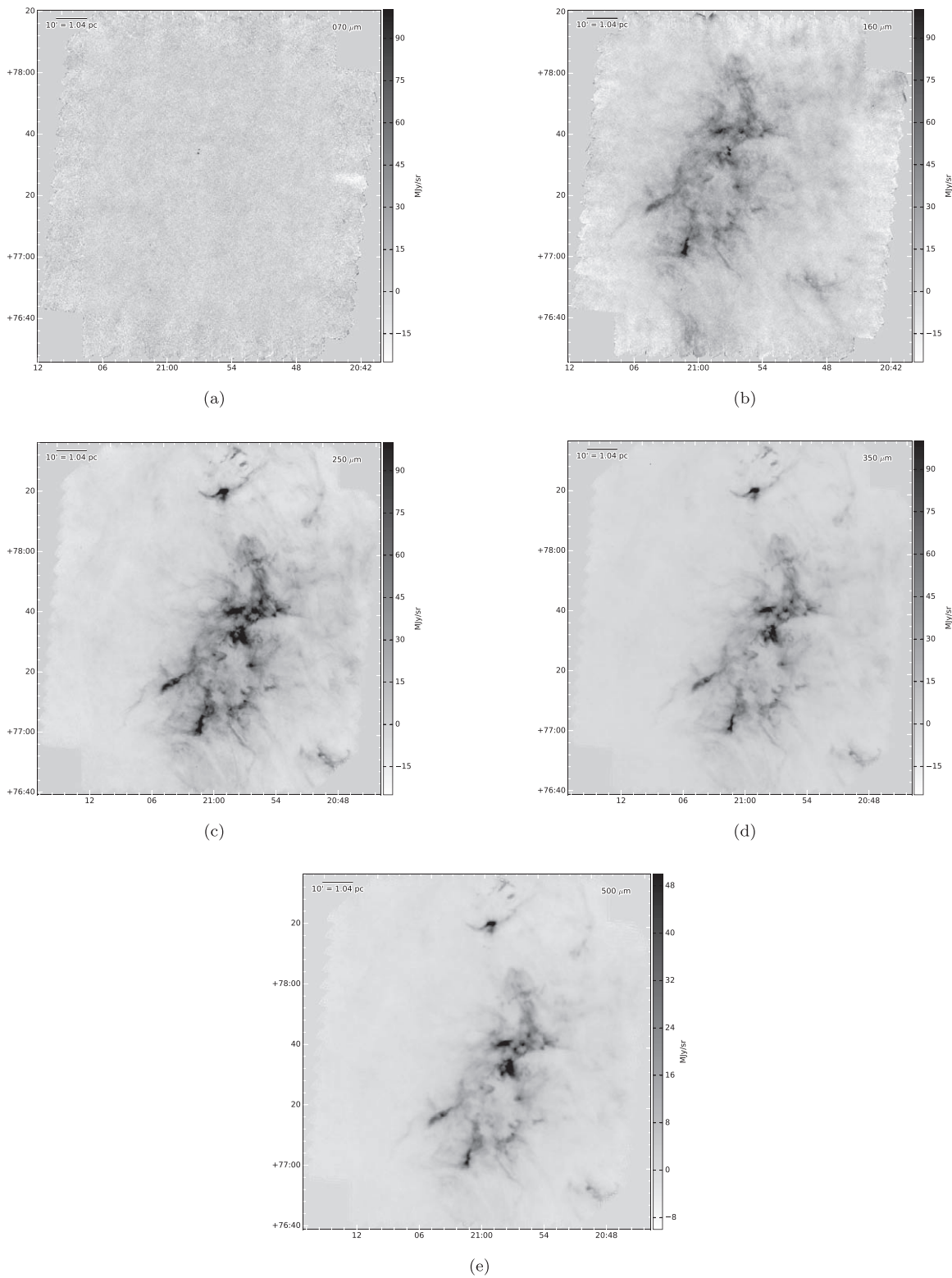
Figure 17. Herschel observations of L1228 at (a) 70 μm, -25 to 100 MJy sr^{-1}; (b) 160 μm, -25 to 100 MJy sr^{-1}; (c) 160 μm, -25 to 100 MJy sr^{-1}; (d) 350 μm, -25 to 100 MJy sr^{-1}; and (e) 500 μm, -10 to 50 MJy sr^{-1}.
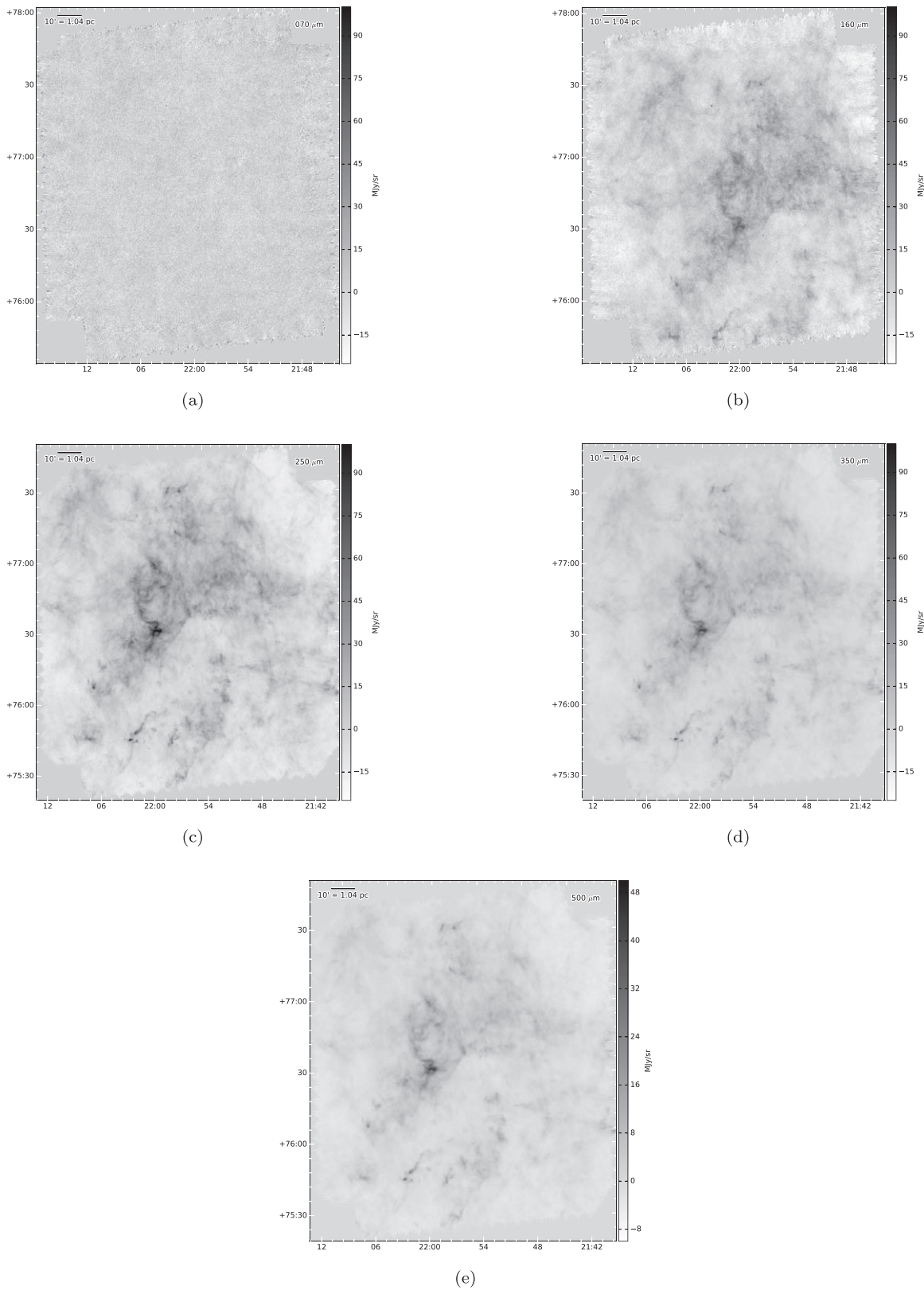
Figure 18. Herschel observations of L1241 at (a) 70 μm, -25 to 100 MJy sr^{-1}; (b) 160 μm, -25 to 100 MJy sr^{-1}; (c) 160 μm, -25 to 100 MJy sr^{-1}; (d) 350 μm, -25 to 100 MJy sr^{-1}; and (e) 500 μm, -10 to 50 MJy sr^{-1}.

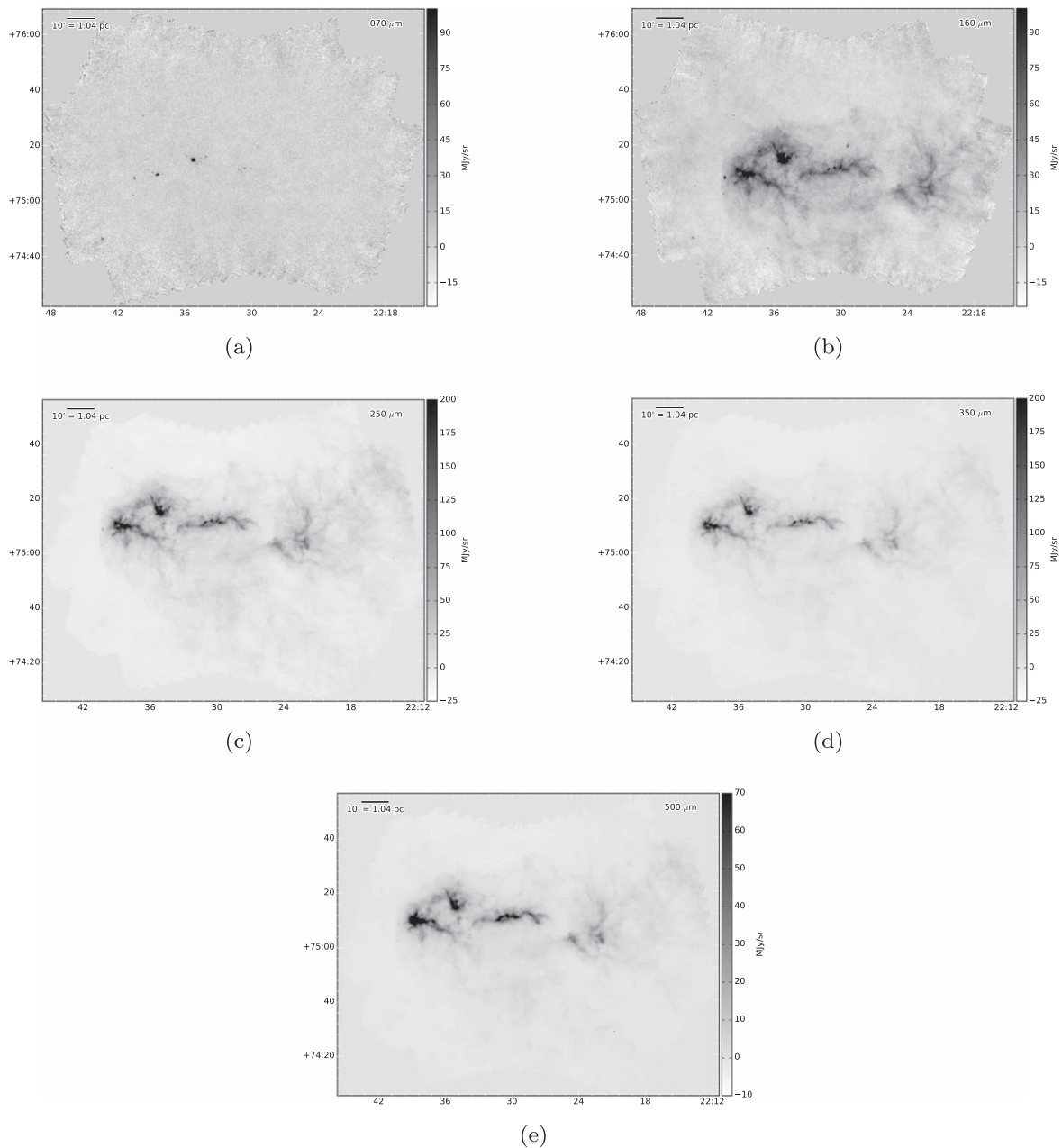**Figure 19.** Herschel observations of L1251 at (a) 70 μm, -25 to 100 MJy sr^{-1}; (b) 160 μm, -25 to 100 MJy sr^{-1}; (c) 160 μm, -25 to 100 MJy sr^{-1}; (d) 350 μm, -25 to 100 MJy sr^{-1}; and (e) 500 μm, -10 to 50 MJy sr^{-1}.

Appendix B
Reliability Criteria for *getsources* Extractions

In this appendix, we list the criteria applied to the list of sources detected by the *getsources* algorithm to select reliable extractions. These criteria are the same as those applied by other HGBS teams to extract reliable sources from Herschel data of other nearby molecular clouds (e.g., Könyves et al. 2015).

The criteria applied to the list of dense cores are as follows:

1. Column density detection significance greater than 5 in the high-resolution column density map ($Sig_{N_{H_2}} > 5$).
2. Global detection significance over all wavelengths greater than 10.

3. Global goodness >1, where goodness is an output quality parameter of *getsources*, combining global signal-to-noise ratio (S/N) and source reliability.
4. Column density measurement S/N > 1 in the high-resolution column density map.
5. Monochromatic detection significance greater than 5 ($Sig_{\lambda} > 5$) in at least two bands between 160 and 500 μm.
6. Flux measurement with S/N > 1 in at least one band between 160 and 500 μm for which the monochromatic detection significance is simultaneously greater than 5.

The criteria applied to the list of YSOs/protostars are as follows:

1. Monochromatic detection significance greater than 5 in the 70 μm band ($\mathrm{Sig}_{070} > 5$).
2. Positive peak and integrated flux densities at 70 μm ($S_{070}^{\mathrm{peak}} > 0$ and $S_{070}^{\mathrm{tot}} > 0$).
3. Global goodness greater than or equal to 1.
4. Flux measurement with S/N > 1.5 in the 70 μm band.
5. FWHM source size at 70 μm smaller than 1.6 times the 70 μm beam size ($\overline{FWHM}_{070} < 1.6 \times 8\farcs4 = 13\farcs44$).
6. Estimated source elongation <1.30 at 70 μm, where source elongation is defined as the ratio of the major- and minor-axis FWHM sizes ($FWHM_{070}^{\mathrm{a}}/FWHM_{070}^{\mathrm{b}} < 1.30$).

Appendix C
Catalogs of Observed and Derived Physical Properties of Cepheus Dense Cores

A catalog of the observed properties of the Cepheus dense cores can be found in online material. Table C1 describes the entries in this catalog by column, with associated units and labels following the HGBS definitions provided by Könyves et al. (2015) or comparably used in the online material header. For each dense core, the catalog includes the host cloud identifier, i.e., its name (Col. 1), the object running number for that cloud (Col. 2), its HGBS source name (Col. 3), and its J2000 position (Cols. 4–9). The HGBS source name is defined with the prefix "HGBS_J" directly followed by a tag given by the sexagesimal coordinates of the J2000 position.

For each of the five Herschel wavelengths, the catalog includes the detection significance (Cols. 10, 20, 30, 40, and 50, respectively). The detection significance is given a special value of 0.0 if the core is not visible in clean single scales. In addition, the catalog lists for each wavelength the peak intensity and error (Cols. 11 ± 12, 21 ± 22, 31 ± 32, 41 ± 42, and 51 ± 52, respectively). Next, the catalog lists for each wavelength the contrast over the local background, i.e., the ratio of the background-subtracted peak intensity to the local background intensity (Cols. 13, 23, 33, 43, and 53, respectively). The catalog then lists the peak flux density at 70, 160, 250, and 350 μm in a 36\farcs3 beam, i.e., the resolution of the Herschel images at 500 μm (Cols. 14, 24, 34, and 44, respectively) and the total integrated flux and error at each wavelength (Cols. 15 ± 16, 25 ± 26, 35 ± 36, 45 ± 46, and 54 ± 55). The catalog also lists for each object its major- and minor-axis FWHM diameters (Cols. 17 and 18, 27 and 28, 37 and 38, 47 and 48, and 56 and 57, respectively) and the position angle of its major axis east of north (Cols. 19, 29, 39, 49, and 58, respectively), where a value of "−1" indicates that no size measurement was possible. The catalog also provides for each object its respective detection significance in the high-resolution column density map (Col. 59); the peak H_2 column density at 18\farcs2 resolution, i.e., the resolution of the Herschel images at 250 μm (Col. 60); the column density contrast over

Table C1
Cepheus Dense Core Observed Properties Catalog Entries

Column	Unit	Description	HGBS Label	Online Material Label
1	⋯	Cloud identifier	⋯	Cloud
2	⋯	Object running number	rNO	Seq
3	⋯	HGBS source name	Core name	Name
4	hr	Hour of R.A. (J2000)	$\mathrm{R.A.}_{2000}(h)$	RAhr
5	m	Minute of R.A. (J2000)	$\mathrm{R.A.}_{2000}(m)$	RAm
6	s	Second of R.A. (J2000)	$\mathrm{R.A.}_{2000}(s)$	RAs
7	°	Degree of decl. (J2000)	$\mathrm{decl.}_{2000}(d)$	DEd
8	′	Arcminute of decl. (J2000)	$\mathrm{decl.}_{2000}(m)$	DEm
9	″	Arcsecond of decl. (J2000)	$\mathrm{decl.}_{2000}(s)$	DEs
10	⋯	Detection significance at 70 μm	Sig_{070}	Signi070
11	Jy beam^{-1}	Peak intensity at 70 μm	S_{070}^{peak}	Sp070
12	Jy beam^{-1}	1σ uncertainty in peak intensity at 70 μm	$S_{070}^{\mathrm{peak,err}}$	e_Sp070
13	⋯	Contrast over local background at 70 μm	$S_{070}^{\mathrm{peak}}/S_{\mathrm{bg}}$	Sp070/Sbg070
14	Jy beam^{-1}	Peak flux density in a 36\farcs3 beam at 70 μm	$S_{070}^{\mathrm{conv,500}}$	Sconv070
15	Jy	Total integrated flux at 70 μm	S_{070}^{tot}	Stot070
16	Jy	1σ uncertainty in total integrated flux at 70 μm	$S_{070}^{\mathrm{tot,err}}$	e_Stot070
17	arcseconds	Major-axis FWHM at 70 μm	$FWHM_{070}^{\mathrm{a}}$	FWHMa070
18	arcseconds	Minor-axis FWHM at 70 μm	$FWHM_{070}^{\mathrm{b}}$	FWHMb070
19	degrees	Position angle of major axis at 70 μm	PA_{070}	PA070
20	⋯	Detection significance at 160 μm	Sig_{160}	Signi160
21	Jy beam^{-1}	Peak intensity at 160 μm	S_{160}^{peak}	Sp160
22	Jy beam^{-1}	1σ uncertainty in peak intensity at 160 μm	$S_{160}^{\mathrm{peak,err}}$	e_Sp160
23	⋯	Contrast over local background at 160 μm	$S_{160}^{\mathrm{peak}}/S_{\mathrm{bg}}$	Sp160/Sbg160
24	Jy beam^{-1}	Peak flux density in a 36\farcs3 beam at 160 μm	$S_{160}^{\mathrm{conv,500}}$	Sconv160
25	Jy	Total integrated flux at 160 μm	S_{160}^{tot}	Stot160
26	Jy	1σ uncertainty in total integrated flux at 160 μm	$S_{160}^{\mathrm{tot,err}}$	e_Stot160
27	arcseconds	Major-axis FWHM at 160 μm	$FWHM_{160}^{\mathrm{a}}$	FWHMa160
28	arcseconds	Minor-axis FWHM at 160 μm	$FWHM_{160}^{\mathrm{b}}$	FWHMb160
29	degrees	Position angle of major axis at 160 μm	PA_{160}	PA160
30	⋯	Detection significance at 250 μm	Sig_{250}	Signi250

Table C1
(Continued)

Column	Unit	Description	HGBS Label	Online Material Label
31	Jy beam^{-1}	Peak intensity at 250 μm	S_{250}^{peak}	Sp250
32	Jy beam^{-1}	1σ uncertainty in peak intensity at 250 μm	$S_{250}^{\mathrm{peak,err}}$	e_Sp250
33	$\cdots$	Contrast over local background at 250 μm	$S_{250}^{\mathrm{peak}}/S_{\mathrm{bg}}$	Sp250/Sbg250
34	Jy beam^{-1}	Peak flux density in a 36″3 beam at 250 μm	$S_{250}^{\mathrm{conv,500}}$	Sconv250
35	Jy	Total integrated flux at 250 μm	S_{250}^{tot}	Stot250
36	Jy	1σ uncertainty in total integrated flux at 250 μm	$S_{250}^{\mathrm{tot,err}}$	e_Stot250
37	arcseconds	Major-axis FWHM at 250 μm	$FWHM_{250}^{\mathrm{a}}$	FWHMa250
38	arcseconds	Minor-axis FWHM at 250 μm	$FWHM_{250}^{\mathrm{b}}$	FWHMb250
39	degrees	Position angle of major axis at 250 μm	PA$_{250}$	PA250
40	$\cdots$	Detection significance at 350 μm	Sig$_{350}$	Signi350
41	Jy beam^{-1}	Peak intensity at 350 μm	S_{350}^{peak}	Sp350
42	Jy beam^{-1}	1σ uncertainty in peak intensity at 350 μm	$S_{350}^{\mathrm{peak,err}}$	e_Sp350
43	$\cdots$	Contrast over local background at 350 μm	$S_{350}^{\mathrm{peak}}/S_{\mathrm{bg}}$	Sp350/Sbg350
44	Jy beam^{-1}	Peak flux density in a 36″3 beam at 350 μm	$S_{350}^{\mathrm{conv,500}}$	Sconv350
45	Jy	Total integrated flux at 350 μm	S_{350}^{tot}	Stot350
46	Jy	1σ uncertainty in total integrated flux at 350 μm	$S_{350}^{\mathrm{tot,err}}$	e_Stot350
47	arcseconds	Major-axis FWHM at 350 μm	$FWHM_{350}^{\mathrm{a}}$	FWHMa350
48	arcseconds	Minor-axis FWHM at 350 μm	$FWHM_{350}^{\mathrm{b}}$	FWHMb350
49	degrees	Position angle of major axis at 350 μm	PA$_{350}$	PA350
50	$\cdots$	Detection significance at 500 μm	Sig$_{500}$	Signi500
51	Jy beam^{-1}	Peak intensity at 500 μm	S_{500}^{peak}	Sp500
52	Jy beam^{-1}	1σ uncertainty in peak intensity at 500 μm	$S_{500}^{\mathrm{peak,err}}$	e_Sp500
53	$\cdots$	Contrast over local background at 500 μm	$S_{500}^{\mathrm{peak}}/S_{\mathrm{bg}}$	Sp500/Sbg500
54	Jy	Total integrated flux at 500 μm	S_{500}^{tot}	Stot500
55	Jy	1σ uncertainty in total integrated flux at 500 μm	$S_{500}^{\mathrm{tot,err}}$	e_Stot500
56	arcseconds	Major-axis FWHM at 500 μm	$FWHM_{500}^{\mathrm{a}}$	FWHMa500
57	arcseconds	Minor-axis FWHM at 500 μm	$FWHM_{500}^{\mathrm{b}}$	FWHMb500
58	degrees	Position angle of major axis at 500 μm	PA$_{500}$	PA500
59	$\cdots$	Detection significance in high-resolution column density map	Sig$_{\mathrm{N_{H_2}}}$	SigniNH2
60	10^{21} cm^{-2}	Peak H$_2$ column density at 18″2 resolution	$N_{\mathrm{H_2}}^{\mathrm{peak}}$	NpH2
61	$\cdots$	Contrast over local background in column density	$N_{\mathrm{H_2}}^{\mathrm{peak}}/N_{\mathrm{H_2}}^{\mathrm{bg}}$	NpH2/NbgH2
62	10^{21} cm^{-2}	Peak H$_2$ column density at 36″3 resolution	$N_{\mathrm{H_2}}^{\mathrm{conv,500}}$	NconvH2
63	10^{21} cm^{-2}	Column density of the local background	$N_{\mathrm{H_2}}^{\mathrm{bg}}$	NbgH2
64	arcseconds	Major-axis FWHM in high-resolution column density map	$FWHM_{\mathrm{NH_2}}^{\mathrm{a}}$	FWHMaNH2
65	arcseconds	Minor-axis FWHM in high-resolution column density map	$FWHM_{\mathrm{NH_2}}^{\mathrm{b}}$	FWHMbNH2
66	degrees	Position angle of major axis in high-resolution column density map	PA$_{\mathrm{NH_2}}$	PANH2
67	$\cdots$	Number of Herschel bands at which object is significantly identified	N_{SED}	NSED
68	$\cdots$	Flag indicating object was also identified by CSAR	CSAR	CSARflag
69	$\cdots$	Core type	Core Type	Type
70	$\cdots$	Closest SIMBAD counterpart, if any	SIMBAD	NSIMBAD
71	$\cdots$	Closest NED counterpart, if any	$\cdots$	NNED
72	$\cdots$	Closest Spitzer counterpart, if any	Spitzer	NSPITZER

(This table is available in its entirety in machine-readable form.)

the background (Col. 61); the peak H$_2$ column density in a 36″3 beam, i.e., the resolution of the Herschel images at 500 μm (Col. 62); the column density of the local background as determined by *getsources* (Col. 63); the major- and minor-axis FWHM diameters and the position angle of the major axis east of north in the high-resolution column density map (Cols. 64–66); and the number of Herschel bands at which the core has been significantly identified, i.e., Sig$_\lambda > 5$ (Col. 67).

In addition, the catalog lists (Col. 68) a flag indicating whether the core was also identified by CSAR, i.e., "2" if the core has a counterpart also found by CSAR within 6″, "1" if no close CSAR counterpart exists but the peak position of a CSAR source is found within the FHWM contour of the core in the high-resolution column density map, or "0" otherwise. Furthermore, the catalog lists (Col. 69) the core type, i.e., starless, (candidate) prestellar, or protostellar. The catalog also lists the closest SIMBAD, NED, and Spitzer counterparts (see Kirk et al. 2009), if any, within 6″ of the Herschel peak position (Cols. 70, 71, and 72, respectively).

Figures 20 and 21 show example thumbnail images of emission at each wavelength and local column density for a robust prestellar core and a protostellar core, respectively. The

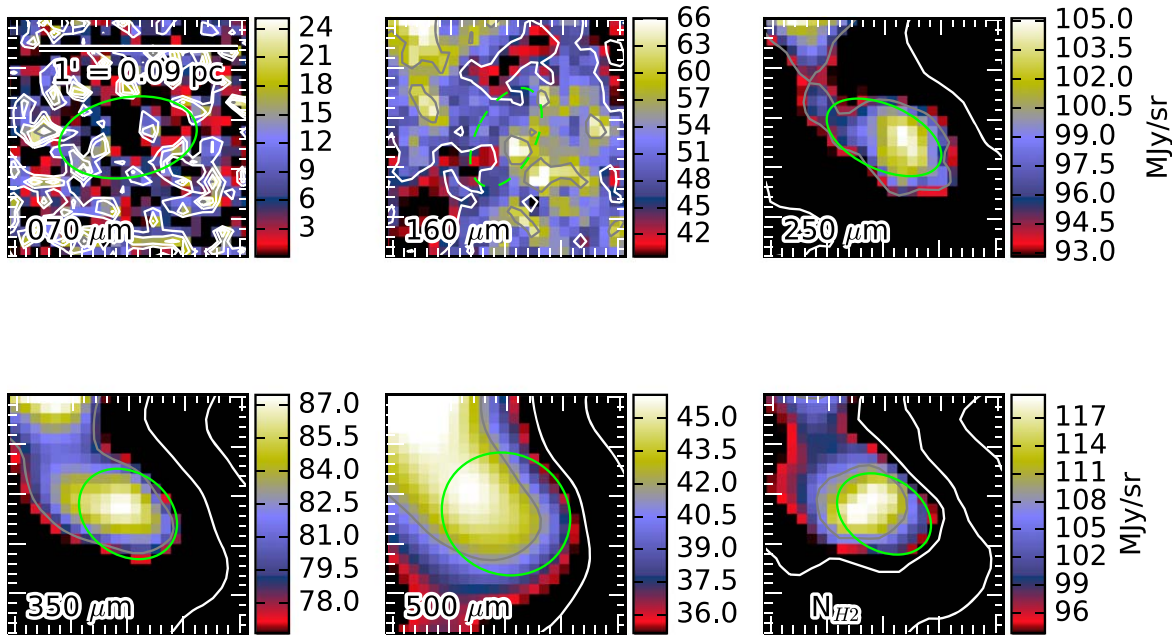## Core Number 15 - RA: 310.77504 Dec: 67.83592

Figure 20. Example thumbnail images of a dense core (L1157-15) at 70 μm (upper left), 160 μm (upper center), 250 μm (upper right), 350 μm (lower left), 500 μm (lower center) and in the high-resolution column density map (lower right). Green ellipses show the extents of the object at each wavelength determined by *getsources*. Based on its mass and size, this object is estimated to be a robust prestellar core.

(The complete figure set (832 images) is available.)

Core Number 1 - RA: 309.7765 Dec: 68.03783
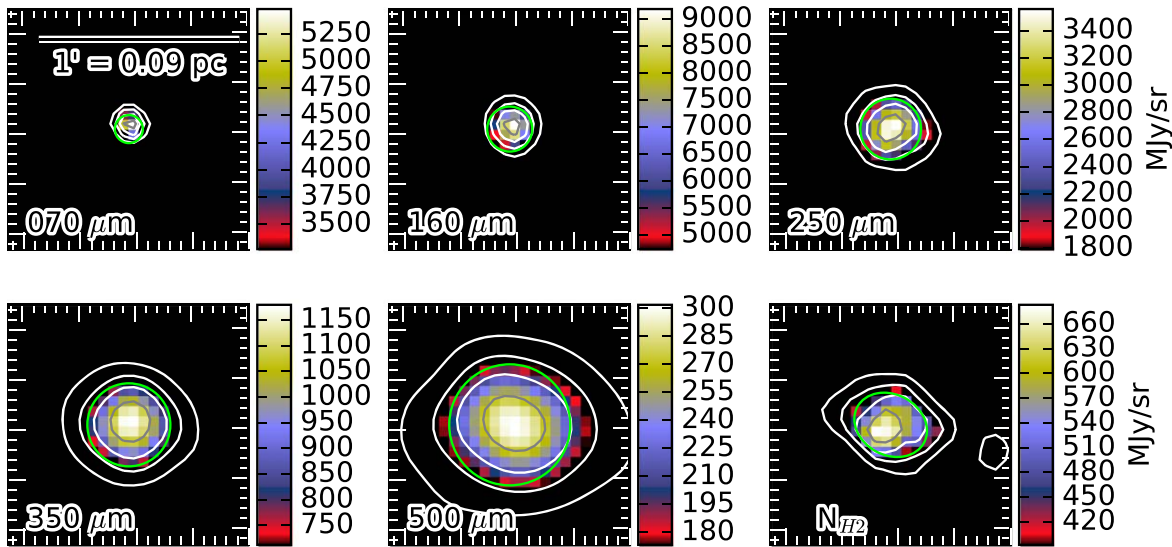
Figure 21. Example thumbnail images of a protostellar core (L1157-1) at 70 μm (upper left), 160 μm (upper center), 250 μm (upper right), 350 μm (lower left), 500 μm (lower center) and in the high-resolution column density map (lower right). Green ellipses show the extent of the objects determined by *getsources*.

full suite of thumbnail images for each dense core is also available in the figure set.

A catalog of the derived physical properties of each Cepheus dense core can be found also in online material. Table C2 describes the entries in this catalog by column, with associated units and labels again following the HGBS definitions provided by Könyves et al. (2015) or comparably used in the online material header. For each dense core, the catalog includes its host cloud identifier (Col. 1), its object running number

(Col. 2), its HGBS source name (Col. 3), and its J2000 coordinates (Cols. 4–9). In addition, the catalog lists each core's deconvolved and observed core radii, each obtained from the geometrical average of the core's major- and minor-axis FWHMs, as measured in the high-resolution column density map, after deconvolution from the 18″2 HPBW of the map and before deconvolution, respectively (Cols. 10 and 11). As noted by Könyves et al. (2015), these values provide estimates of the outer radius of the core when it can be

Table C2
Cepheus Dense Core Derived Physical Properties Catalog Entries

Column	Unit	Description	HGBS Label	Online Material Label
1	⋯	Cloud identifier	⋯	Cloud
2	⋯	Object running number	rNO	Seq
3	⋯	HGBS source name	Core Name	Name
4	hr	Hour of R.A. (J2000)	$R.A._{2000}(hr)$	RAhr
5	m	Minute of R.A. (J2000)	$R.A._{2000}(m)$	RAm
6	s	Second of R.A. (J2000)	$R.A._{2000}(s)$	RAs
7	°	Degree of decl. (J2000)	$decl._{2000}(d)$	DEd
8	′	Arcminute of decl. (J2000)	$decl._{2000}(m)$	DEm
9	″	Arcsecond of decl. (J2000)	$decl._{2000}(s)$	DEs
10	pc	Deconvolved core radius	R_{core}^{decon}	Rd
11	pc	Observed core radius	R_{core}^{obs}	Robs
12	$M_\odot$	Estimated core mass	M_{core}	Mcore
13	$M_\odot$	1σ uncertainty on estimated core mass	M_{core}^{err}	e_Mcore
14	K	Dust temperature	T_{dust}	Tdust
15	K	1σ uncertainty on dust temperature	T_{dust}^{err}	e_Tdust
16	10^{21} cm^{-2}	Peak column density at 36″3 resolution	$N_{H_2}^{peak}$	NH2peak
17	10^{21} cm^{-2}	Average column density before deconvolution	$N_{H_2}^{ave}$	NH2av
18	10^{21} cm^{-2}	Average column density after deconvolution	$N_{H_2}^{ave,d}$	NH2avd
19	10^{4} cm^{-3}	Peak volume density at 36″3 resolution	$n_{H_2}^{peak}$	nH2peak
20	10^{4} cm^{-3}	Average volume density before deconvolution	$n_{H_2}^{ave}$	nH2av
21	10^{4} cm^{-3}	Average volume density after deconvolution	$n_{H_2}^{ave,d}$	nH2avd
22	⋯	BE mass ratio	α_{BE}	alphaBE
23	⋯	Core type	Core Type	Coretype
24	⋯	Comments	Comments	Com

(This table is available in its entirety in machine-readable form.)

approximately described by a Gaussian distribution, as is the case for a BE spheroid. Next, the catalog lists for each core its estimated mass and the associated 1σ uncertainty (Cols. 12 and 13) and its dust temperature and the associated 1σ uncertainty (Cols. 14 and 15), following standard HGBS practices. (Note that the 1σ uncertainties include statistical errors including calibration uncertainties but not uncertainties in dust opacity.) Next, the catalog lists for each core its peak column density at 36″3 resolution, as derived from a graybody SED fit to the core peak flux densities measured at a common 36″3 resolution at all wavelengths (Col. 16). Furthermore, the catalog lists the average column density measured before and after deconvolution, equal to $(M_{core}/\pi R_{core}^2)(1/\mu m_H)$, where R_{core} is the core radius either before or after deconvolution, respectively, $\mu = 2.8$, and m_H is the mass of the hydrogen atom (Cols. 17 and 18). The catalog then includes the beam-averaged peak volume density of each core at 36″3 resolution (Col. 19), derived from the peak column density and assuming a Gaussian spherical distribution, i.e., $n_{H_2}^{peak} = (\sqrt{4\ln 2/\pi})(N_{H_2}^{peak}/\overline{FWHM}_{500})$. In addition, the catalog lists the average volume density measured before and after deconvolution, equal to $(M_{core}/(4/3)\pi R_{core}^3)(1/\mu m_H)$, where, as before, R_{core} is the core radius either before or after deconvolution, respectively (Cols. 20 and 21). Finally, the catalog lists the BE mass ratio $\alpha_{BE} = M_{BE,crit}/M_{core}$ (Col. 22), the core type (starless, (candidate) prestellar, or protostellar; Col. 23), and comments (Col. 24). For the latter, if a graybody SED was unable to be fit to the core flux densities, an entry of "no_SED_fit" is given.

ORCID iDs

James Di Francesco ⓘ https://orcid.org/0000-0002-9289-2450
Jared Keown ⓘ https://orcid.org/0000-0003-2628-0250
Philippe André ⓘ https://orcid.org/0000-0002-3413-2293
Vera Könyves ⓘ https://orcid.org/0000-0002-3746-1498
Peter Martin ⓘ https://orcid.org/0000-0002-5236-3896
Stefano Pezzuto ⓘ https://orcid.org/0000-0001-7852-1971
Eleonora Fiorellino ⓘ https://orcid.org/0000-0002-5261-6216
Milena Benedettini ⓘ https://orcid.org/0000-0002-3597-7263
Nicola Schneider ⓘ https://orcid.org/0000-0003-3485-6678
Pedro Palmeirim ⓘ https://orcid.org/0000-0002-0590-7416
Jason M. Kirk ⓘ https://orcid.org/0000-0002-4552-7477
Derek Ward-Thompson ⓘ https://orcid.org/0000-0003-1140-2761

References

André, P., Di Francesco, J., Ward-Thompson, D., et al. 2014, in Protostars and Planets VI, ed. H. Beuther et al. (Tucson, AZ: Univ. Arizona Press), 27
André, P., Men'shchikov, A., Bontemps, S., et al. 2010, A&A, 518, L102
Arzoumanian, D., André, P., Didelon, P., et al. 2011, A&A, 529, L6
Arzoumanian, D., André, P., Könyves, V., et al. 2019, A&A, 621, A42
Balog, Z., Müller, T., Nielbock, M., et al. 2014, ExA, 37, 129
Bendo, G. J., Griffin, M. J., Bock, J. J., et al. 2013, MNRAS, 433, 3062
Benedettini, M., Pezzuto, S., Schisano, E., et al. 2018, A&A, 619, A52
Benedettini, M., Schisano, E., Pezzuto, S., et al. 2015, MNRAS, 453, 2036
Bernard, J. P., Paradis, D., Marshall, D. J., et al. 2010, A&A, 518, L88
Bohlin, R. C., Savage, B. D., & Drake, J. F. 1978, ApJ, 224, 132
Bonnor, W. B. 1956, MNRAS, 116, 351
Bresnahan, D., Ward-Thompson, D., Kirk, J. M., et al. 2018, A&A, 615, A125
Chabrier, G. 2005, in The Initial Mass Function: From Salpeter 1955 to 2005, ed. E. Corbelli, F. Palla, & H. Zinnecker (Dordrecht: Springer), 41

Di Francesco, J., Evans, N. J. I., Caselli, P., et al. 2007, in Protostars and Planets V, ed. B. Reipurth, D. Jewitt, & K. Keil (Tucson, AZ: Univ. Arizona Press), 17

Dunham, M. M., Crapsi, A., Evans, N. J. I., et al. 2008, ApJS, 179, 249

Dzib, S. A., Loinard, L., Ortiz-León, G. N., Rodríguez, L. F., & Galli, P. A. B. 2018, ApJ, 867, 151

Ebert, R. 1955, ZAp, 37, 217

Fiorellino, E., Elia, D., André, Ph., et al. 2020, MNRAS, in press

Fischera, J., & Martin, P. G. 2012, A&A, 542, A77

Griffin, M. J., Abergel, A., Abreu, A., et al. 2010, A&A, 518, L3

Griffin, M. J., North, C. E., Schulz, B., et al. 2013, MNRAS, 434, 992

Hildebrand, R. H. 1983, QJRAS, 24, 267

Inutsuka, S.-i., & Miyama, S. M. 1997, ApJ, 480, 681

Kauffmann, J., Bertoldi, F., Bourke, T. L., Evans, N. J. I., & Lee, C. W. 2008, A&A, 487, 993

Kirk, J. M., Ward-Thompson, D., Di Francesco, J., et al. 2009, ApJS, 185, 198

Kirk, J. M., Ward-Thompson, D., Palmeirim, P., et al. 2013, MNRAS, 432, 1424

Könyves, V., André, P., Arzoumanian, D., et al. 2020, A&A, 635, A34

Könyves, V., André, P., Men'shchikov, A., et al. 2015, A&A, 584, A91

Kroupa, P. 2001, MNRAS, 322, 231

Kun, M., Kiss, Z. T., & Balog, Z. 2008, in Star Forming Regions in Cepheus, ed. B. Reipurth, Vol. 4 (San Francisco, CA: ASP), 136

Ladjelate, B., André, Ph., Könyves, V., et al. 2020, A&A, 638, A74

Marsh, K. A., Kirk, J. M., André, P., et al. 2016, MNRAS, 459, 342

Men'shchikov, A. 2013, A&A, 560, A63

Men'shchikov, A., André, P., Didelon, P., et al. 2012, A&A, 542, A81

Ortiz-León, G. N., Loinard, L., Dzib, S. A., et al. 2018, ApJL, 869, L33

Ostriker, J. 1964, ApJ, 140, 1056

Ott, S. 2011, in ASP Conf. Ser. 442, HIPE, HIPE, Hooray!, ed. I. N. Evans et al. (San Francisco, CA: ASP), 347

Palmeirim, P., André, P., Kirk, J., et al. 2013, A&A, 550, A38

Pattle, K., Ward-Thompson, D., Kirk, J. M., et al. 2017, MNRAS, 464, 4255

Pezzuto, S., Benedettini, M., Di Francesco, J., et al. 2020, A&A, in press

Pilbratt, G. L., Riedinger, J. R., Passvogel, T., et al. 2010, A&A, 518, L1

Poglitsch, A., Waelkens, C., Geis, N., et al. 2010, A&A, 518, L2

Roussel, H. 2013, PASP, 125, 1126

Roy, A., André, P., Arzoumanian, D., et al. 2015, A&A, 584, A111

Salpeter, E. E. 1955, ApJ, 121, 161

Skrutskie, M. F., Cutri, R. M., Stiening, R., et al. 2006, AJ, 131, 1163

Soler, J. D. 2019, A&A, 629, A96

Ward-Thompson, D., André, P., Crutcher, R., et al. 2007, in Protostars and Planets V, ed. B. Reipurth, D. Jewitt, & K. Keil (Tucson, AZ: Univ. Arizona Press), 33

Williams, J. P., de Geus, E. J., & Blitz, L. 1994, ApJ, 428, 693

Yonekura, Y., Dobashi, K., Mizuno, A., Ogawa, H., & Fukui, Y. 1997, ApJS, 110, 21